Monthly Notices of the ROYAL ASTRONOMICAL SOCIETY

MNRAS **472,** 4878–4899 (2017) doi:10.1093/mnras/stx2305
Advance Access publication 2017 September 6

Predicting emission line fluxes and number counts of distant galaxies for cosmological surveys

F. Valentino,[1,2★] E. Daddi,[2] J. D. Silverman,[3] A. Puglisi,[4,5] D. Kashino,[6] A. Renzini,[7] A. Cimatti,[8,9] L. Pozzetti,[10] G. Rodighiero,[4] M. Pannella,[11] R. Gobat[12] and G. Zamorani[10]

[1]*Dark Cosmology Centre, Niels Bohr Institute, University of Copenhagen, Juliane Maries Vej 30, DK-2100 Copenhagen, Denmark*
[2]*Laboratoire AIM-Paris-Saclay, CEA/DSM-CNRS-Université Paris Diderot, Irfu/Service d'Astrophysique, CEA Saclay, Orme des Merisiers, F-91191 Gif sur Yvette, France*
[3]*Kavli Institute for the Physics and Mathematics of the Universe, The University of Tokyo, Kashiwa, Japan 277-8583 (Kavli IPMU, WPI)*
[4]*Dipartimento di Fisica e Astronomia, Università di Padova, Vicolo dell'Osservatorio 2, I-35122 Padova, Italy*
[5]*ESO, Karl-Schwarschild-Strasse 2, D-85748 Garching bei München, Germany*
[6]*Department of Physics, ETH Zürich, Wolfgang-Pauli-strasse 27, CH-8093 Zürich, Switzerland*
[7]*INAF Osservatorio Astronomico di Padova, Vicolo dell'Osservatorio 5, I-35122 Padova, Italy*
[8]*Department of Physics and Astronomy (DIFA), Università di Bologna, Via Gobetti 93/2, I-40129 Bologna, Italy*
[9]*INAF – Osservatorio Astrofisico di Arcetri, Largo E. Fermi 5, I-50125 Firenze, Italy*
[10]*INAF Osservatorio Astronomico di Bologna, Via Gobetti 93/3, I-40129, Bologna, Italy*
[11]*Department of Physics, Ludwig-Maximilians-Universität, Scheinerstr. 1, D-81679 München, Germany*
[12]*School of Physics, Korea Institute for Advanced Study, Hoegiro 85, Dongdaemun-gu, Seoul 02455, Republic of Korea*

Accepted 2017 September 4. Received 2017 September 4; in original form 2017 May 16

ABSTRACT

We estimate the number counts of line emitters at high redshift and their evolution with cosmic time based on a combination of photometry and spectroscopy. We predict the Hα, Hβ, [O II], and [O III] line fluxes for more than 35 000 galaxies down to stellar masses of $\sim 10^9$ M$_\odot$ in the COSMOS and GOODS-S fields, applying standard conversions and exploiting the spectroscopic coverage of the FMOS-COSMOS survey at $z \sim 1.55$ to calibrate the predictions. We calculate the number counts of Hα, [O II], and [O III] emitters down to fluxes of 1×10^{-17} erg cm^{-2} s^{-1} in the range $1.4 < z < 1.8$ covered by the FMOS-COSMOS survey. We model the time evolution of the differential and cumulative Hα counts, steeply declining at the brightest fluxes. We expect $\sim$9300–9700 and $\sim$2300–2900 galaxies deg^{-2} for fluxes $\geq 1 \times 10^{-16}$ and $\geq 2 \times 10^{-16}$ erg cm^{-2} s^{-1} over the range of $0.9 < z < 1.8$. We show that the observed evolution of the main sequence of galaxies with redshift is enough to reproduce the observed counts variation at $0.2 < z < 2.5$. We characterize the physical properties of the Hα emitters with fluxes $\geq 2 \times 10^{-16}$ erg cm^{-2} s^{-1} including their stellar masses, UV sizes, [N II]/Hα ratios and Hα equivalent widths. An aperture of $R \sim R_e \sim 0.5$ arcsec maximizes the signal-to-noise ratio for a detection, whilst causing a factor of $\sim 2 \times$ flux losses, influencing the recoverable number counts, if neglected. Our approach, based on deep and large photometric data sets, reduces the uncertainties on the number counts due to the selection and spectroscopic samplings whilst exploring low fluxes. We publicly release the line flux predictions for the explored photometric samples.

Key words: galaxies: distances and redshifts – galaxies: high-redshift – galaxies: star formation – galaxies: statistics – large-scale structure of Universe – cosmology: observations.

★ E-mail: francesco.valentino@nbi.ku.dk

1 INTRODUCTION

As supported by several independent pieces of evidence, mysterious 'dark' components dominate the mass and energy budget of the Universe, adding up to ∼96 per cent of the total energy density in the current Λ cold dark matter (ΛCDM) cosmological framework. In particular, a 'dark energy' is considered the engine of the accelerated expansion of the Universe, as suggested by and investigated through the study of supernovae in galaxies up to $z \sim 1$ (Riess et al. 1998; Schmidt et al. 1998; Perlmutter et al. 1999). On the other hand, 'dark matter' counteracts the effect of dark energy, braking the expansion via the gravitational interaction. As a result, the geometry of our Universe is regulated by the delicate compromise between these two components.

The distribution of galaxies on large scales offers crucial insights on the nature of both these dark components and constitutes a test for the theory of General Relativity, one of the pillars of modern physics. In particular, wiggle patterns in galaxy clustering, the so-called baryonic acoustic oscillations (BAOs), provide a standard ruler to measure the stretch and geometry of the Universe and to put constraints on dark energy independently of the probe provided by supernovae. However, the detection of the BAOs is bound to the precision with which we derive the position of galaxies in the three-dimensional space and to the collection of vast samples of objects. The necessity of accurate redshifts to detect BAOs is motivating the launch of intense spectroscopical campaigns to pinpoint millions of galaxies in the sky both from the ground [i.e. BOSS, WiggleZ, and the forthcoming Prime Focus Spectrograph (PFS), Dark Energy Spectroscopic Instrument (DESI), and Multi-Object Optical Near-infrared Spectrograph surveys; Blake et al. 2011; Dawson et al. 2013; Levi et al. 2013; Cirasuolo et al. 2014; Takada et al. 2014] and in space with dedicated missions, such as Euclid (Laureijs 2009) and WFIRST (Green et al. 2012; Spergel et al. 2015). In particular, taking full advantage of high-precision imaging and absence of atmospheric absorption, the space missions will probe critical epochs up to $z \sim 2$, when the dark energy starts manifesting its strongest effects and accurate weak lensing measurements can map the distribution of dark matter in the Universe. Observationally, these missions will apply a slitless spectroscopy technique to estimate redshifts from bright nebular lines and, notably, from Hα emission, a primary tracer of hydrogen, generally ionized by young O- and B-type stars or active galactic nuclei (AGN). Moreover, even if at low resolution, the spectroscopic characterization of such a large sample of star forming and active galaxies will be a gold mine for the study of galaxy evolution over time. Therefore, a prediction of the number of potentially observable galaxies is required to optimize the survey strategies, in order to have the maximal scientific return from these missions.

As typically done, the predicted number counts over wide redshift intervals are determined modelling the evolution of the luminosity function (LF) of Hα emitters, reproducing the available samples of spectroscopic and narrow-band imaging data sets (Geach et al. 2010; Colbert et al. 2013; Mehta et al. 2015; Sobral et al. 2015; Pozzetti et al. 2016, and references therein). However, this method generally relies on empirical extrapolations of the time evolution of the parameters describing the LF, and it is bound to limited statistics. Observationally, narrow-band imaging surveys benefit from the large sky areas they can cover, at the cost of significant contamination issues and the thin redshift slices probed, making them prone to the uncertainties due to cosmic variance. On the other hand, despite the limited covered areas, spectroscopic surveys directly probe larger redshift intervals, combing large cosmic volumes, reducing the impact of cosmic variance. Here, we propose an alternative method based on photometry of star-forming galaxies (SFGs), covering their whole spectral energy distribution (SED), in synergy with spectroscopy for a subsample of them. We show that spectroscopic observations allow for an accurate calibration of the Hα fluxes expected for typical main-sequence (MS) SFGs (Noeske et al. 2007; Daddi et al. 2007). As a consequence, we can take advantage of much larger photometric samples of galaxies currently available in cosmological fields to estimate the number counts of line emitters. We test the validity of this approach exploiting large photometric samples in the COSMOS and GOODS-S fields, and calibrating the Hα flux predictions against the FMOS-COSMOS survey at $z \sim 1.55$ (Silverman et al. 2015). Flux predictions for the Hα and other relevant emission lines ([O II] λ3727 Å, Hβ λ4861 Å, and [O III]i λ5007 Å) and the photometric properties of this sample are released in a catalogue. We, then, compute the number counts of Hα, [O II] and [O III] emitters in the redshift range of $1.4 < z < 1.8$ covered by the FMOS-COSMOS survey and we predict the evolution of the Hα counts with redshift, modelling the evolution of the normalization of the MS and including the effect of the luminosity distance. We argue that this is enough to reproduce the observed trends over the redshift range of $0.2 < z < 2.5$. Admittedly, this process relies on a few assumptions and is affected by uncertainties and limitations we discuss in the article, but it is physically motivated and it has the general advantage of sensibly decreasing the errors due to low number statistics, overcoming some of the observational limitations of current spectroscopic surveys from the ground. It also benefits from a better control of selection effects than studies based on the detection of emission lines only. Coupled with the canonical approach based on the evolution of the Hα LF, our method strives to obtain a more solid estimate of the integrated Hα counts. Finally, we present a detailed physical characterization of the brightest Hα emitters in terms of stellar mass, redshift distribution, dust extinction, nebular line ratios, and Hα equivalent widths (EWs), key elements to prepare realistic simulations of the primary population of galaxies observable by forthcoming wide spectroscopic surveys.

This paper is organized as follows: in Section 2, we present the photometric and the FMOS-COSMOS spectroscopic samples used to estimate the number counts of emitters and calibrate the prediction of line fluxes, respectively. In Section 3, we introduce the procedure to calculate Hα, Hβ, [O II] and [O III] fluxes. We characterize the photometric and spectroscopic properties of a sample of bright Hα emitters visible in future surveys in Section 4. In Section 5, we compute the number counts of Hα, [O II] and [O III] emitters for the redshift range covered by FMOS-COSMOS. In the same section, we extend the predictions on the Hα number counts to broader redshift intervals probed by the forthcoming cosmological missions. Finally, we discuss our results, caveats, and possible developments in Section 6, presenting the concluding remarks in Section 7. Unless stated otherwise, we assume a ΛCDM cosmology with $\Omega_{\rm m} = 0.3$, $\Omega_{\Lambda} = 0.7$, and $H_0 = 70\,{\rm km\,s^{-1}\,Mpc^{-1}}$ and a Salpeter initial mass function (IMF; Salpeter 1955). All magnitudes are expressed in the AB system.

2 DATA AND SAMPLE SELECTION

In this section, we introduce the photometric samples of SFGs drawn from the COSMOS and GOODS-S fields. We further present the FMOS-COSMOS spectroscopic survey data set used to calibrate the predictions of Hα fluxes, the latter being based on the star formation rates (SFRs) from SED fitting. Unless specified otherwise, the 'COSMOS' and 'GOODS-S photometric' samples will be treated

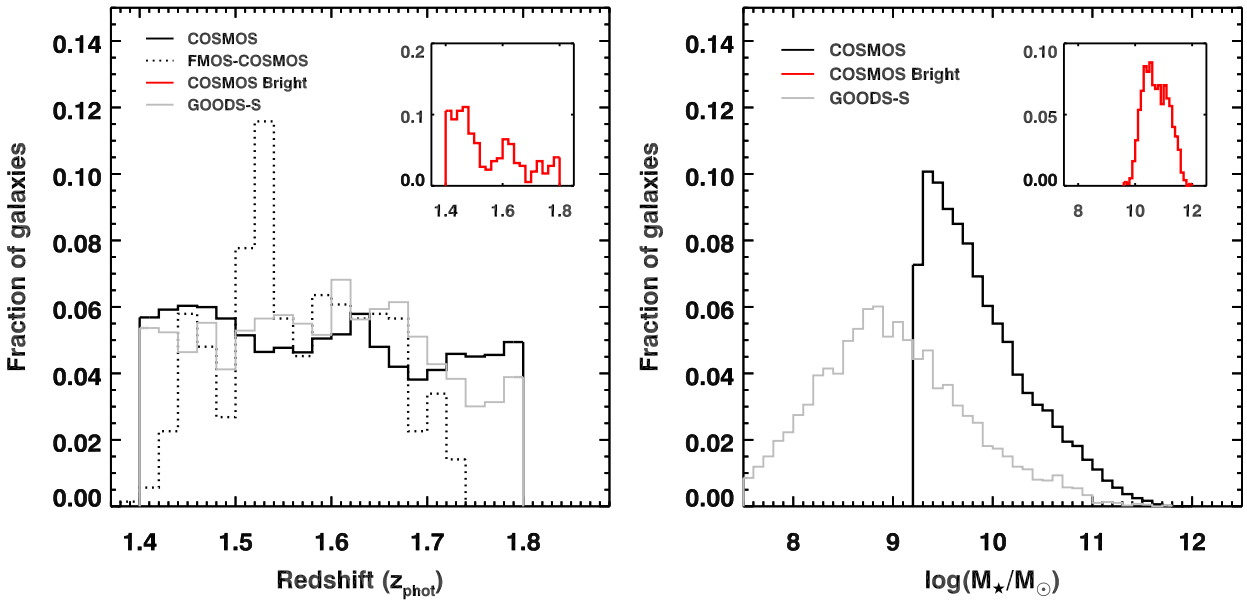

Figure 1. Properties of the photometric samples. Left: The solid black and grey histograms show the photometric redshift distributions of the SFGs we selected in COSMOS and GOODS-S, respectively. The black dotted histogram shows the FMOS-COSMOS spectroscopic redshift distribution of Hα emitters. The histograms are normalized to the total number of objects in each sample. The red histogram in the inset shows the normalized distribution for a subsample of 750 galaxies with predicted Hα fluxes $\geq 2 \times 10^{-16}$ erg cm^{-2} s^{-1} in COSMOS (Section 4). Right: Stellar mass distributions for the same COSMOS (black) and GOODS-S (grey) samples, and for the subsample of bright Hα emitters in COSMOS (red histogram).

separately and compared when possible. We will refer to the calibration data set as the 'FMOS-COSMOS' or the 'spectroscopic' sample.

2.1 The COSMOS photometric sample

We selected the target sample from the latest COSMOS photometric catalogue by Laigle et al. (2016), including the UltraVISTA-DR2 photometry. We identified SFGs according to the *NUV*−*r*, *r*−*J* criterion (Williams et al. 2009; Ilbert et al. 2013), and retained only the objects falling in the photometric redshift range of $1.4 < z < 1.8$, resulting in a sample of 31 193 galaxies with stellar masses of $M_\star \geq 10^{9.2}$ M$_\odot$. X-ray-detected AGN from Civano et al. (2016) were flagged (PHOTOZ = 9.99 in Laigle et al. 2016) and removed from our sample, since we could not reliably predict their line fluxes. We show the photometric redshift and the stellar-mass distributions in Fig. 1. The distribution of z_{phot} is flat in the redshift range we considered. On the other hand, the $M_\star$ distribution shows a substantial drop at $M_\star \sim 10^{9.2}$ M$_\odot$. The COSMOS sample is formally ∼90 per cent complete down to $M_\star \geq 10^{9.8}$ M$_\odot$ in this redshift range, corresponding to a cut at $K_s = 24$ mag in the shallowest regions covered by UltraVISTA (Laigle et al. 2016). However, Fig. 1 shows that the completeness limit can be pushed to a lower value for the sample of SFGs we selected, simply because low-mass galaxies are generally blue. In this case, this extended photometric sample allows for putting constraints on the number counts at low fluxes (Section 5), a regime usually inaccessible for purely spectroscopic analyses. Notice that we limit the number counts to a flux of 5×10^{-17} erg cm^{-2} s^{-1}, above which the sample of Hα emitters is virtually flux complete. Seventy-eight per cent of the whole sample above this flux threshold have a stellar mass above the mass completeness limit, and this fraction rises to 95 per cent for Hα fluxes above 1×10^{-16} erg cm^{-2} s^{-1} used as a reference for the differential number counts in Section 5.2. Therefore, the results on the brightest tail of emitters are not affected by the drop of the stellar mass distribution in the sample.

We selected the $1.4 < z < 1.8$ redshift interval to match the one of the FMOS-COSMOS survey (Section 2.2). We adopted the stellar masses from the catalogue by Laigle et al. (2016), computed with LEPHARE (Ilbert et al. 2006) and assuming Bruzual & Charlot (2003) stellar population synthesis models, a composite star formation history (SFR $\propto \tau^{-2} t e^{-t/\tau}$), solar and half-solar metallicities, and Calzetti et al. (2000) or Arnouts et al. (2013) extinction curves. We homogenized the IMFs applying a 0.23 dex correction to the stellar masses in the catalogue, computed with the prescription by Chabrier (2003). We then re-modelled the SED from the rest-frame UV to the *Spitzer*/IRAC 3.6 μm band with the code HYPERZ (Bolzonella, Miralles & Pelló 2000), using the same set of stellar population models and a Calzetti et al. (2000) reddening law, but assuming constant SFRs. We chose the latter since they proved to reconcile the SFR estimates derived independently from different indicators and to consistently represent the MS of SFGs (Rodighiero et al. 2014). We checked the resulting SFRs and dust attenuation A_V from SED modelling against estimates from the luminosity at 1600 Å only (Kennicutt 1998) and UV β-slope (Meurer, Heckman & Calzetti 1999). In both cases, we obtain consistent results within the scatter and the systematic uncertainties likely dominating these estimates. A tail of ∼8 per cent of the total COSMOS sample shows SFRs (UV) ∼ 0.15 dex lower than SFR (SED), but at the same time, they exhibit A_V(UV) ∼ 0.1 mag lower than A_V (SED). However, these objects do not deviate anyhow appreciably from the distribution of predicted Hα fluxes computed in Section 3, nor in stellar masses or photometric redshifts, as confirmed by a Kolmogorov–Smirnov test. We, thus, retain these galaxies in the analysis. SFRs derived from the rest-frame UV range only and dust extinctions from the modelling of the full SED extended to the *Spitzer*/IRAC 3.6 μm band proved to robustly predict Hα fluxes, not requiring any secondary corrections. We adopt these estimates in the rest of this work.

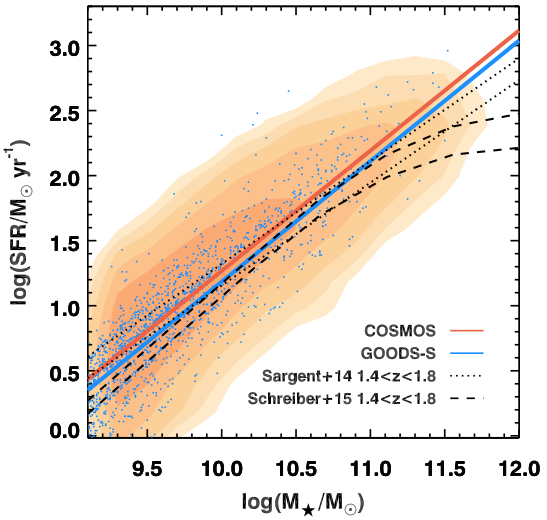

Figure 2. Main sequence of SFGs at $z \sim 1.5$. Orange contours mark density contours of our sample of NUVrJ-selected SFGs at $1.4 < z < 1.8$ and with $M_\star \geq 10^{9.2}$ M$_\odot$ from the COSMOS field. Objects similarly selected and modelled in GOODS-S are indicated with blue points (Pannella et al., private communication). Best fit to the COSMOS and GOODS-S data are shown with orange and blue solid lines, respectively. Analytical parametrizations of the MS by Sargent et al. (2014) and Schreiber et al. (2015) for $z = 1.4$ and $z = 1.8$ are marked by dotted and dashed dark lines, respectively.

2.1.1 A control sample in GOODS-South

We further check the consistency of our compilation of stellar masses and SFRs in COSMOS comparing it with a sample of SFGs in GOODS-S. This field benefits from a deeper coverage of the rest-frame UV range, allowing for a better constraint of the SFRs down to lower levels, and to put constraints on the tail of Hα emitters at low fluxes and masses, not recoverable in COSMOS. We, thus, selected a sample of 3858 galaxies with $M_\star \geq 10^{7.5}$ M$_\odot$ at $1.4 < z < 1.8$, applying the same criteria listed above. The 90 per cent mass completeness limit is $M_\star = 10^9$ M$_\odot$ and 1813 galaxies fall above this threshold. We show the normalized redshift and stellar mass distribution of the GOODS-S in Fig. 1. A two-tail Kolmogorov–Smirnov test shows that the redshift distributions are compatible. The different mass completeness limits between COSMOS and GOODS-S are evident from the right-hand panel, with a tail of GOODS-S objects extending below $M_\star = 10^9$ M$_\odot$. A Kolmogorov–Smirnov test on the raw data shows that the distributions are consistent with the hypothesis of being drawn from the same parent sample, especially when limiting the analysis to the COSMOS mass completeness threshold. We then modelled the SEDs of objects in GOODS-S applying the same recipes we adopted for the COSMOS sample (Pannella et al., private communication). As shown in Fig. 2, we consistently recover the MS of galaxies in COSMOS and GOODS-S. We also find a good agreement with the analytical parametrizations of the MS by Sargent et al. (2014) and Schreiber et al. (2015).

2.2 The FMOS-COSMOS survey

The FMOS-COSMOS survey is a near-infrared spectroscopic survey designed to detect Hα and [N II]$\lambda\lambda$6549, 6584 Å in galaxies at $1.43 < z < 1.74$ in the H band with the Fiber Multi-Object Spectrograph (FMOS; Kimura et al. 2010) on the Subaru Telescope. An integration of 5 h allows for the identification of emission lines of total flux down to 4×10^{-17} erg cm^{-2} s^{-1} at 5σ with the H-long grism ($R \sim 2600$). Galaxies with positive Hα detections have been re-imaged with the J-long grism ($R \sim 2200$) to detect [O III]$\lambda\lambda$4959, 5007 Å and Hβ emission lines to characterize the properties of the ionized interstellar medium (ISM; Zahid et al. 2014; Kashino et al. 2017a). For a detailed description of the target selection, observations, data reduction, and the creation of the spectroscopic catalogue, we refer the reader to Silverman et al. (2015). For the scope of this work, i.e. the calibration of the Hα fluxes predictions from the photometry, we selected only the objects with a signal-to-noise ratio $\geq$5 on the observed Hα flux. Their spectroscopic redshifts distribution is consistent with the one of photometric redshifts of the COSMOS sample discussed in Section 2.1 (Fig. 1). We mention here that the primary selection relies on Hα flux predictions based on continuum emission similar to the ones reported in the next section. This strategy might result in a bias against starbursting sources with anomalously large line EWs, strongly deviating from the average stellar mass, SFR and extinction trends. Whilst this is unlikely to affect the most massive galaxies, given their large dust content, we could miss starbursting galaxies at the low-mass end ($M_\star \lesssim 10^{9.5}$ M$_\odot$), where the survey is not complete (Section 6.3). Moreover, since we preferentially targeted massive galaxies and J-band observations aimed at identifying the [O III] emission followed a positive Hα detection, we lack direct observational probe of sources with large [O III]/Hα ratios at low masses and Hα fluxes. However, as we further discuss in Section 3.3, this potential bias is likely mitigated by the extrapolation of the analytical form we adopt to model the line ratios and predict [O III] fluxes.

Note that ~44 per cent of the initial FMOS-COSMOS targets were eventually assigned a spectroscopic redshift (Silverman et al. 2015). The success rate when predicting line fluxes and redshifts is likely higher considering that ~25 per cent of the wavelength range is removed by the FMOS OH-blocking filter. The remaining failures can be ascribed to bad weather observing conditions; telescope tracking issues and fibre flux losses; high instrumental noise in the outer part of the spectral range; errors on photometric redshifts (11 per cent of objects are missed due to stochastic errors); the uncertainties on the dust content of galaxies; significant intra-population surface brightness variations. We also note that the misidentification of fake signal and/or non-Hα line may occur in ~10 per cent of the all line detections (Kashino et al. 2017b). The latter is a rough estimate based on four discordant spectroscopic redshift between the FMOS-COSMOS and the zCOSMOS(-deep) surveys (Lilly et al. 2007) out of 28 galaxies in common, assuming that the zCOSMOS determinations are correct. This line misidentification fraction may be overestimated, given the small sampling rate of zCOSMOS-deep at the range of the FMOS-COSMOS survey. Since we use the spectroscopic observations mainly to calibrate the flux predictions from photometry (Section 3), line misidentification does not strongly affect our results. In fact, either they cause flux predictions to be widely different from observations and, thus, they are excluded from the calibration sample (Fig. 3); or, if by a lucky coincidence, the predicted Hα fluxes fall close to the observed values of a different line, they spread the distribution of the observed-to-predicted flux ratios (Fig. 3), naturally contributing to the final error budget we discuss later on. Notice also that the success rate increases up to ~60 per cent for predicted Hα fluxes $\geq 2 \times 10^{-16}$ erg cm^{-2} s^{-1}, a relevant flux regime further discussed in detail in the rest of the article.

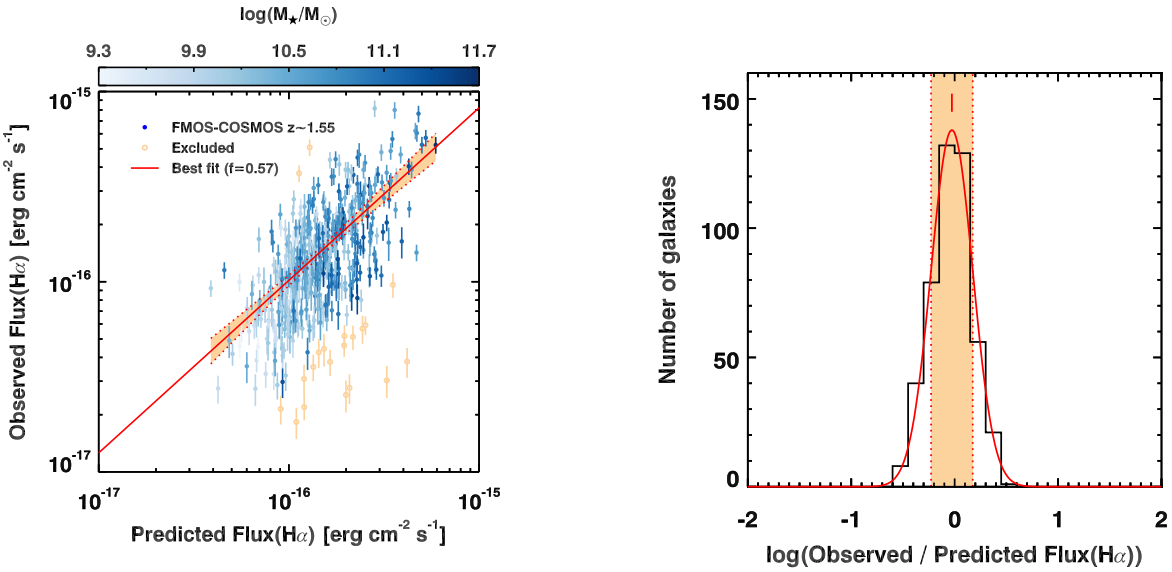

Figure 3. Prediction of total H α fluxes for SFGs in COSMOS. Left: Predicted and observed total, aperture corrected, H α fluxes for 486 sources detected at $\geq 5\sigma$ in the spectroscopic follow-up with FMOS. Blue circles mark the 440 sources used to optimize the f value. Blue colours scale as the stellar mass. Orange empty circles represent sources with widely different predictions and observations, excluded from the calculation of the f factor. The red solid and dotted lines represent the best fit to the logarithmic data and the associated 95 per cent confidence interval. Right: The black line shows the distribution of the observed-to-predicted H α flux ratios in logarithmic scale. The best Gaussian fitting is overplotted in red. The red tick and the orange-shaded area mark the mean and the 1σ standard deviation of the best Gaussian fit.

3 PREDICTION OF LINE FLUXES FROM PHOTOMETRY

In this section, we introduce the method we applied to predict the nebular line emission from the photometry of the samples presented above. The expected line fluxes are released in a publicly available catalogue.

3.1 H α fluxes

For each source in the photometric sample, we computed the expected *total* observed H α flux based on SFRs and dust attenuation estimated in Section 2.1. We converted the SFR into H α flux following Kennicutt (1998), and we applied a reddening correction converting the $E_{\rm star}(B-V)$ for the stellar component into $E_{\rm neb}(B-V)$ for the nebular emission by dividing by $f = E_{\rm star}(B-V)/E_{\rm neb}(B-V)$. We computed f minimizing a posteriori the difference between the observed and expected total H α fluxes from the FMOS-COSMOS survey presented in Kashino et al. (2017a). Therefore, here f assumes the role of a fudge factor to empirically predict H α fluxes as close as possible to observations. Assigning a physical meaning to f is prone to several uncertainties (Puglisi et al. 2016), and it is beyond the scope of this work. The minimization is based on 486 galaxies in the spectroscopic sample with an observed H α flux $\gtrsim 2 \times 10^{-17}$ erg cm^{-2} s^{-1} detected at $\geq 5\sigma$ (Fig. 3). We verified that the value of f is not biased by low-SN detections or by a small subset of very bright sources, excluding objects in the 10th and 90th percentiles of the distribution of predicted H α fluxes. Moreover, the results do not change imposing FLAG ≥ 2 and a lower signal-to-noise cut of 3 on the observed H α fluxes from FMOS spectroscopy. Sources with divergent predictions and observations were excluded by applying a 2.5σ clipping on the ratios between observed and predicted H α fluxes, leaving 440 galaxies available for the minimization procedure. These ratios are log-normally distributed, with a standard deviation of 0.19 dex (Fig. 3). The dispersion is widely dominated by the $\sim$50 per cent fibre losses and the ensuing uncertainties on the aperture corrections for the FMOS observations (Silverman et al. 2015). A 0.17 dex dispersion is ascribable to this effect, whilst the remaining 0.1 dex is partly intrinsic, due to the different star formation time-scales traced by UV and H α light, and partly owing to the systematic uncertainties of the SED modelling.

Applying this technique, we obtain $f = 0.57 \pm 0.01$, with a scatter of 0.23. A consistent result is retrieved comparing the observed SFR (UV) and SFR (H α) (Kashino et al. 2013). The value of f is higher than the one normally applied for local galaxies ($f = 0.44 \pm 0.03$, Calzetti et al. 2000), consistently with recent results for high-redshift galaxies (Kashino et al. 2013; Pannella et al. 2015; Puglisi et al. 2016). Note that we estimated $E_{\rm star}(B-V)$ using the Calzetti et al. (2000) reddening law, whilst we adopted the Cardelli, Clayton & Mathis (1989) prescription with $R_{\rm V} = 3.1$ to compute $E_{\rm neb}(B-V)$, analogously to what reported in the original work by Calzetti et al. (2000), where they used the similar law by Fitzpatrick (1999). Using the Calzetti et al. (2000) reddening curve to compute both the stellar and nebular extinction would result in higher values of f for local ($f = 0.58$) and $z \sim 1.55$ galaxies ($f = 0.76 \pm 0.01$).

Adopting $f = 0.57$, the best fit to the logarithmic data is $\log(\mathrm{H}\alpha_{\rm obs}) = (0.91 \pm 0.01)\log(\mathrm{H}\alpha_{\rm pred}) + (-1.48 \pm 0.19)$ with a correlation coefficient $\rho = 0.9998$. The uncertainties represent the statistical error in the fitting procedure, whilst the scatter of the relation is $\sigma = 0.19$ dex (Fig. 3). Assuming a fixed slope of 1, the best fit is $\log(\mathrm{H}\alpha_{\rm obs}) = \log(\mathrm{H}\alpha_{\rm pred}) + (-0.009 \pm 0.002)$. Secondary corrections as a function of $M_\star$ or $E(B-V)$ are not necessary, since the $\log(\mathrm{H}\alpha_{\rm obs}/\mathrm{H}\alpha_{\rm pred})$ ratio is constant and consistent with 0 over the ranges probed by the FMOS-COSMOS detections ($10^{9.3} \leq M_\star \leq 10^{11.7}$ M$_\odot$, $E(B-V) \leq 0.84$ mag). Eventually, we adopted $f = 0.57$ to predict the H α and other line fluxes (see below) both in COSMOS and GOODS-S, assuming its validity over the entire

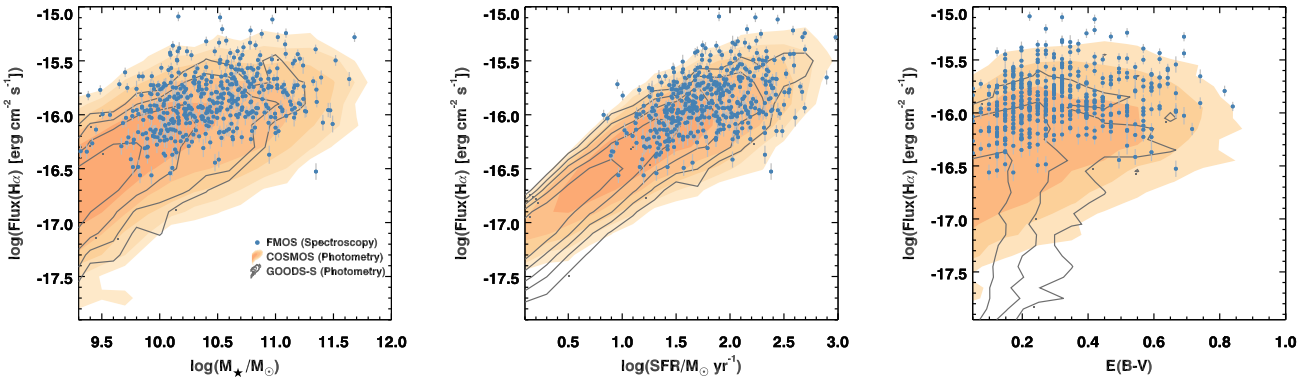

Figure 4. Predicted H α fluxes as a function of SED-derived quantities. The orange and grey contours show the density contours of the COSMOS and GOODS-S photometric samples, respectively. The blue points mark the position of spectroscopically confirmed objects in the FMOS-COSMOS survey. The H α fluxes are integrated and not corrected for reddening. Left: Stellar mass versus H α fluxes. Centre: SFR versus H α fluxes. Right: $E(B-V)$ versus H α fluxes.

stellar mass and reddening ranges covered by these samples. We also assume that the uncertainties on the predicted H α fluxes derived for the FMOS-COSMOS sample are applicable for galaxies in GOODS-S. In Fig. 4, we show the correlations amongst the predicted H α fluxes and the SED-derived stellar masses, SFRs, and reddening $E(B-V)$ for the COSMOS and GOODS-S photometric samples. We also plot the spectroscopically confirmed objects from the FMOS-COSMOS survey. The large $E(B-V)$ at high stellar masses compensates the increase of the SFR on the MS, so that the $M_\star$-observed H α flux relation is flat above $M_\star \sim 10^{10}$ M$_\odot$, ensuring high stellar mass completeness above this threshold when observing down to H α fluxes of 1×10^{-17} erg cm^{-2} s^{-1}. Notice that the FMOS-COSMOS observations are biased towards the lower $E(B-V)$, as expected from the initial selection (Section 2.2) and the fact that less dusty objects are naturally easier to detect. Finally, the uncertainties on $E(B-V)$ are included in the correlation of SFR into observed H α fluxes shown in the central panel.

3.2 H β fluxes

We computed H β fluxes rescaling the H α values for the different extinction coefficients k_λ and assuming the intrinsic ratio H β = H α/2.86 (Osterbrock & Ferland 2006). Note that the stellar Balmer absorption might impact the final observed H β flux. We, thus, compute a stellar mass dependent correction following Kashino et al. (2017a):

$$f_{\rm corr} = \max[1,\, 1.02 + 0.30 \log(M_\star/10^{10}\,{\rm M}_\odot)], \quad (1)$$

where $f_{\rm corr}$ corresponds to a correction up to 50 per cent. We report this term in the released catalogue for completeness so to compute the observed, Balmer-absorbed fluxes, if needed. However, the correction is not applied to the total H β fluxes shown in the rest of this work.

3.3 [O III] fluxes

We predict [O III] fluxes adopting a purely empirical approach calibrated against the average spectra of the FMOS-COSMOS SFGs described in Kashino et al. (2017a). The observed log ([O III]/H β) ratio anticorrelates with log (M$_\star$), as shown in Fig. 5 (mass-excitation diagram; Juneau et al. 2011). Being H β and [O III] close in wavelength, their ratio is not deeply affected by reddening corrections. Here, we predict [O III] fluxes from H β forcing the line

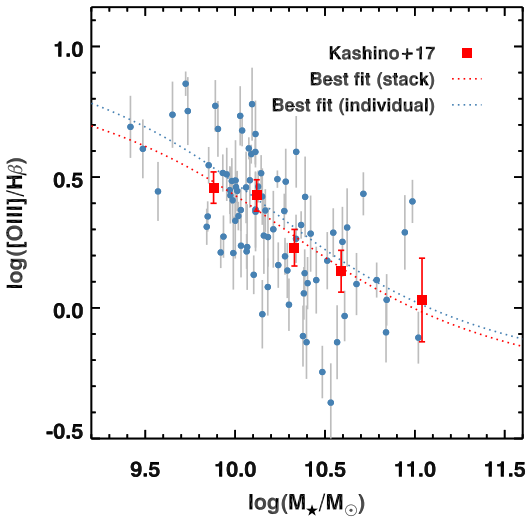

Figure 5. [O III]/H β ratio as a function stellar mass for the FMOS-COSMOS survey at $z \sim 1.5$. Blue points mark the observed galaxies in the FMOS-COSMOS survey with 3σ detections of both the [O III] and H β lines. Grey error bars represent the 1σ uncertainties on the ratio estimates. Red squares mark the average values for SFGs in the FMOS-COSMOS survey as derived in Kashino et al. (2017a). The red and blue lines indicate the best fit to the stacked values and individual sources, respectively.

ratio to follow a simple arctangent model fitting the stacked values. The best-fitting model is $\log([{\rm O\,III}]/{\rm H}\,\beta) = (0.30 \pm 0.37) + (0.48 \pm 0.12)\arctan\{-[\log(M_\star/{\rm M}_\odot) - (10.28 \pm 0.84)]\}$. Fitting the individual sources does not impact the main conclusions of this work. Note that these predictions are valid only for the redshift window $1.4 < z < 1.8$, where a significant evolution of the [O III]/H β ratio is not expected (Cullen et al. 2016). Notice also that the number of secure individual 3σ detections of both [O III] and H β is restrained (84 galaxies) and that the line ratio suffers from a significant scatter.

The comparison between predicted and observed [O III] fluxes is shown in Fig. 6. The best fit to the logarithmic data is $\log([{\rm O\,III}]_{\rm obs}) = (1.00 \pm 0.03)\log([{\rm O\,III}]_{\rm pred}) + (0.08 \pm 0.45)$ with a correlation coefficient $\rho = 0.99995$. The best model is derived from 181 galaxies with a $\geq$3σ detection of [O III] from our FMOS-COSMOS sample, after applying a 2σ clipping to remove 22 strong

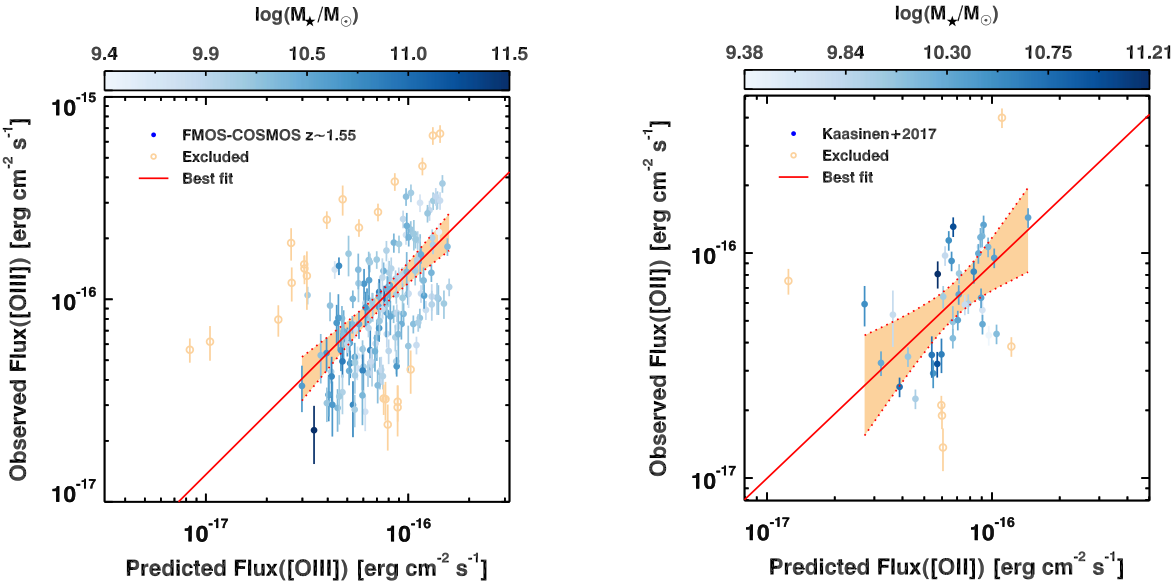

Figure 6. Oxygen lines flux predictions. Left: Blue circles mark predicted and observed [O III] fluxes from a sample of 159 galaxies with 3σ detections in the FMOS-COSMOS survey. Symbols are colour coded according to stellar masses. The red solid line and orange shaded area indicate the best fit to the data and its 95 per cent confidence interval. Orange empty circles have been excluded from the fit. Right: Blue circles mark predicted and observed [O II] fluxes from a sample of 37 galaxies with 3σ detections from Kaasinen et al. (2017). Symbols are colour coded according to stellar masses. The red solid line and orange shaded area indicate the best fit to the data and its 95 per cent confidence interval. Orange empty circles have been excluded from the fit.

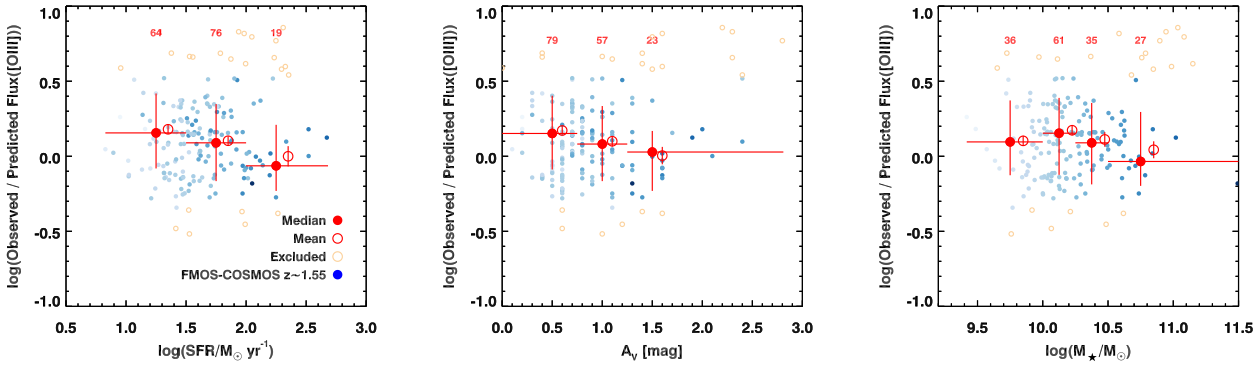

Figure 7. Observed-to-predicted [O III] flux ratios as a function of SED-derived quantities. In each panel, blue filled circles show the $[\mathrm{O\,III}]_{\mathrm{obs}}/[\mathrm{O\,III}]_{\mathrm{pred}}$ ratios against SED-derived SFRs (left), A_{V} (centre), and stellar masses $M_{\star}$ (right) for the sample of galaxies with an [O III] flux measurement from the FMOS-COSMOS survey. Symbols are colour coded according to stellar masses as in Fig. 6. Orange empty circles have been excluded applying the 2σ clipping described in Section 3.3. The red filled circles and vertical bars represent the median of $[\mathrm{O\,III}]_{\mathrm{obs}}/[\mathrm{O\,III}]_{\mathrm{pred}}$ ratios in subsequent bins and the $\pm1\sigma$ percentiles (15.84, 84.16 per cent). The horizontal bars show the width of each bin, selected based on the enclosed number of objects (reported in red in the three panels) and the typical systematics affecting SED modelling. Red open circles and bars represent the mean of line ratios in each bin and its standard error ($=\sigma/\sqrt{N}$), where N is the number of objects per bin.

outliers. Note that the flux range covered by FMOS [O III] observations is more limited than for Hα. The distribution of observed-to-predicted [O III] fluxes has a width of $\sigma = 0.25$ dex, dominated by the uncertainties on FMOS aperture corrections, as for the Hα line. Fig. 7 shows that we underpredict the [O III] flux by up to ∼0.1 dex for galaxies with low SFR ($\lesssim$30 $\mathrm{M_{\odot}\,yr^{-1}}$) and low A_{V} ($\lesssim$0.8 mag) from the SED fitting, but we do not find any evident dependence on stellar mass, even if FMOS-COSMOS [O III] observations probe only the $M_{\star} \gtrsim 10^{9.5}$ $\mathrm{M_{\odot}}$ regime. Since we allowed for a lower signal-to-noise ratio to detect [O III] emission than Hα fluxes in order to increase the sample statistics, here we adopted a stricter clipping threshold to eliminate outliers. In particular, AGN contamination likely boosts [O III] fluxes in the latter, massive objects (median $M_{\star} = 10^{10.8}$ $\mathrm{M_{\odot}}$), causing systematically larger observed fluxes than predicted for inactive SFGs. We applied the same calibration to the galaxies in GOODS-S and assumed that the uncertainties derived from the spectroscopic sample in COSMOS applies to GOODS-S, too. Note that the [O III] flux and the [O III]/Hβ ratio are sensitive to the presence of AGN. Moreover, the number of bright [O III] emitters with low masses is significantly larger than for the Hα line, since the [O III]/Hβ increases for decreasing masses. This is particularly relevant for the GOODS-S sample. As mentioned in Section 2.2, the FMOS-COSMOS survey does not probe the low-mass, high [O III]/Hβ regime, where line ratios up to 0.8–1 are typically observed (Henry et al. 2013). However, extrapolating the best-fitting models shown in Fig. 5 down to $M_{\star} \sim 10^{8}$ $\mathrm{M_{\odot}}$, we cover the range of observed ratios, likely mitigating a potential bias against large [O III] fluxes.

3.4 [O II] fluxes

[O II] might be used as a SFR tracer (Kennicutt 1998; Kewley, Geller & Jansen 2004; Talia et al. 2015), even if its calibration depends on secondary parameters such as the metal abundance. Here, we simply assume $L([\mathrm{O\,II}]) = L(\mathrm{H}\,\alpha)$ (Kewley et al. 2004) and the extinction coefficient $k([\mathrm{O\,II}]) = 4.771$ from the Cardelli et al. (1989) reddening curve ($R_V = 3.1$). In Fig. 6, we show the predicted [O II] fluxes against a sample of 43 spectroscopic measurements in COSMOS from Kaasinen et al. (2017) in common with our catalogue. After applying a 2σ clipping to the $[\mathrm{O\,II}]_{\mathrm{obs}}/[\mathrm{O\,II}]_{\mathrm{pred}}$ flux ratios, the best fit to the relation between these two quantities is $\log([\mathrm{O\,II}]_{\mathrm{obs}}) = (0.95 \pm 0.06)\log([\mathrm{O\,II}]_{\mathrm{pred}}) + (-0.83 \pm 0.92)$, with a correlation coefficient $\rho = 0.999\,96$. The width of the distribution of the ratios $[\mathrm{O\,II}]_{\mathrm{obs}}/[\mathrm{O\,II}]_{\mathrm{pred}}$ is $\sigma \sim 0.22$ dex. We applied the same method to the sample in GOODS-S. Also in this case, the stricter clipping threshold than for H α fluxes (Section 3.1) compensates for the lower signal-to-noise limit allowed for [O II] detections, so to increase the size of the available sample. Applying a 5σ detection threshold and a 2.5σ clipping to [O II] observed fluxes results in a similar final object selection to the one presented above.

We note that a similar approach was applied by Jouvel et al. (2009) to simulate emission lines for a mock sample of objects based on the observed SEDs of galaxies in COSMOS. In their work, Jouvel et al. (2009) based the flux predictions assuming [O II] as a primary tracer of SFR and on a set of fixed line ratios. However, [O II] shows secondary dependences on other parameters such as metallicity, even if in first approximation it traces the current SFR. Moreover, the line ratios significantly change with redshift. Furthermore, a proper treatment of the dust extinction is fundamental to derive reliable nebular line fluxes, introducing a conversion between the absorption of the stellar continuum and of the emission lines. Here, we exploited the updated photometry in the same field and GOODS-S, and we tied our predictions to direct spectroscopic observations of a large sample of multiple lines in high-redshift galaxies, the target of future surveys. We primarily estimated the H α fluxes, a line directly tracing hydrogen ionized by young stars and brighter than [O II], thus accessible for larger samples of galaxies spanning a broader range of SFRs and masses. Predictions for oxygen lines emission were directly compared to observations as well.

4 A SAMPLE OF BRIGHT H α EMITTERS AT $z \sim 1.5$

The sensitivity to emission lines achieved by the FMOS-COSMOS and similar spectroscopic surveys is an order-of-magnitude deeper than what expected for forthcoming large surveys (i.e. Euclid wide survey: $\geq 2 \times 10^{-16}$ erg cm^{-2} s^{-1}, 3.5σ; WFIRST: ≥ 0.5–1×10^{-16} erg cm^{-2} s^{-1} for extended sources, 3σ, figs 2–15 of Spergel et al. 2015). Therefore, the physical characterization of the population of bright H α emitters is a key feature in the current phase of preparation for these missions. Here, we have the opportunity to achieve this goal for a fairly large sample of galaxies, exploiting both photometric and spectroscopic data.

4.1 Spectroscopy: line ratios and EWs

The general spectroscopic properties of the FMOS-COSMOS sample are detailed in Kashino et al. (2017a). Here, we focus on a subset of 135 bright sources with total, observed (i.e. corrected for aperture effects, but not for extinction) H α fluxes $\geq 2 \times 10^{-16}$ erg cm^{-2} s^{-1} from their catalogue. First, we visually inspected and manually refitted the FMOS spectra of these sources. We, then, stacked the individual spectra, applying a 5σ clipping at each wavelength. The clipping does not introduce evident biases: the resulting spectrum is fully consistent both with an optimally weighted average and a median spectrum. The average spectrum and the associated uncertainty, estimated through Jackknife and Monte Carlo techniques, are shown in Fig. 8. From this spectrum, we derived H α, [N II], [S II]$\lambda\lambda$6717, 6731 Å, and continuum emission fluxes for the population of bright emitters. Note that [S II] lines are not in the observed wavelength range for galaxies at $1.67 < z < 1.74$.

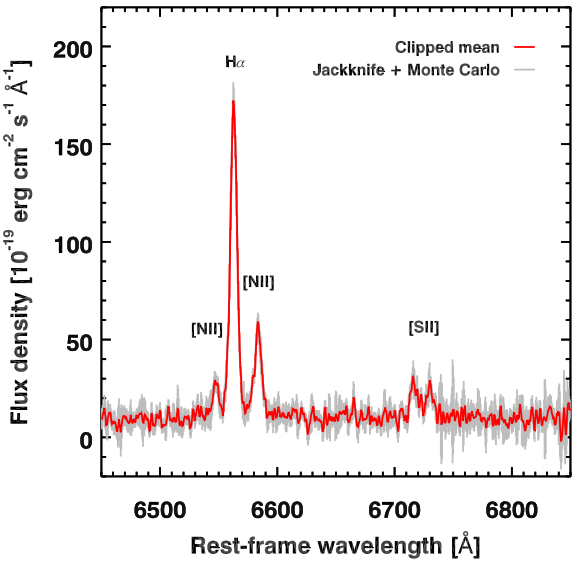

Figure 8. Average spectrum of bright H α emitters from the FMOS-COSMOS survey. The red line marks the clipped average spectrum of 135 individual line emitters with aperture corrected, observed H α fluxes $\geq 2 \times 10^{-16}$ erg cm^{-2} s^{-1} from the catalogue by Kashino et al. (2017a). The grey line shows the associated uncertainty estimated with Monte Carlo and Jackknife techniques.

The left-hand panel of Fig. 9 shows the BPT diagram for a subsample of 39 bright emitters in the FMOS-COSMOS sample with coverage of H β and [O III]. The bright emitters at lower [N II]/Hα ratios are mainly distributed around the average locus of the FMOS-COSMOS sample down to the detection limit of $\geq 4 \times 10^{-17}$ erg cm^{-2} s^{-1} (Kashino et al. 2017a). At ratios above $\log([\mathrm{N\,II}]/\mathrm{H}\,\alpha) \gtrsim -0.5$, bright H α emitters show higher [O III]/H β ratios, possibly due to contamination by AGN, which dominate the line emission in some extreme cases. However, there are not evident trends between the position in the BPT and the H α flux of these bright emitters, as shown by the colour bar. The sample is also offset with respect to the average locus of a sample of 6638 low-redshift galaxies ($0.04 < z < 0.2$) selected from the Sloan Digital Sky Survey DR7 (Abazajian et al. 2009) with well-constrained [O III]/H β and [N II]/H α ratios (Juneau et al. 2014) and with an intrinsic H α luminosity corresponding to fluxes $\geq 4 \times 10^{-17}$ erg cm^{-2} s^{-1} at $z = 1.55$. This shows that the offset in the BPT diagram is not merely due to selection effects (Juneau et al. 2014; Kashino et al. 2017a). Nine out of 39 emitters ($\sim$23 per cent) are classified as AGN according to the criterion by Kewley et al. (2013) at $z \sim 1.55$, and this partly results from the selection of *Chandra* detected sources to complement the main colour selection for the FMOS-COSMOS survey (Silverman

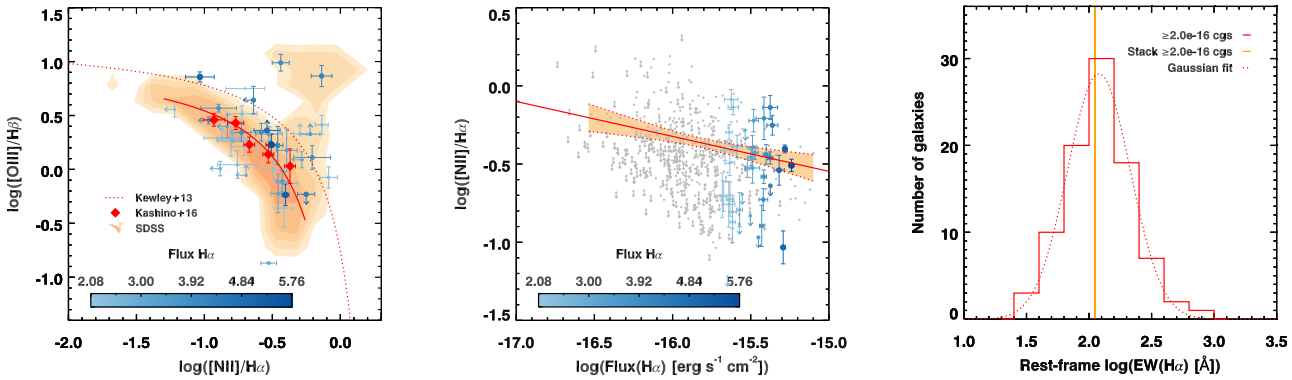

Figure 9. Spectroscopic properties of bright H α emitters at $z \sim 1.5$. Left: BPT diagram for spectroscopically confirmed emitters with H α flux $\geq 2 \times 10^{-16}$ erg cm^{-2} s^{-1} from the FMOS-COSMOS survey. The blue solid circles mark bright emitters. The colour intensity scales as the H α flux in units of 10^{-16} erg cm^{-2} s^{-1} reported in the colour bar. The red diamonds and solid line mark the average location of the FMOS-COSMOS sample of SFGs with total H α flux $\geq 4 \times 10^{-17}$ erg cm^{-2} s^{-1} and the best fit by Kashino et al. (2017a). The red dotted line indicates the limiting curve dividing SFGs and AGN at $z = 1.55$ as parametrized in Kewley et al. (2013). The orange shaded area marks the location of SDSS galaxies with an intrinsic H α luminosity corresponding to a total H α flux of $\geq 4 \times 10^{-17}$ erg cm^{-2} s^{-1} at $z = 1.55$. Centre: [N II]/H α ratios as a function of the total observed H α flux for the spectroscopic FMOS-COSMOS sample. The blue solid circles mark bright H α emitters in the BPT in the left-hand panel. The colour intensity scales as the H α flux in units of 10^{-16} erg cm^{-2} s^{-1} reported in the colour bar. Grey dots and arrows mark the position of the rest of the FMOS-COSMOS spectroscopic sample described in Kashino et al. (2017a). The red solid line indicates the best fit to the data. The orange area and the red dotted lines mark the 95 per cent confidence limits of the fit. Right: The red histogram shows the distribution of rest-frame log [EW(H α)] for spectroscopically confirmed emitters with H α flux $\geq 2 \times 10^{-16}$ erg cm^{-2} s^{-1}. The red dotted line marks the best Gaussian fit to the distribution. The orange band indicates the 1σ confidence limit around the value estimated from the stacked spectrum in Fig. 8.

et al. 2015). In Fig. 9, we show how log ([N II]/H α) apparently anti-correlates with observed H α fluxes. The best fit is log ([N II]/H α)= (-0.22 ± 0.02) log (H α) $- (3.90 \pm 0.26)$ (correlation coefficient $\rho = 0.999\,83$). However, this correlation is naturally affected by observational biases and disappears when stacking [N II] non-detections (Kashino et al. 2017a). The mean ratio log ([N II]/H α) of the subsample of 91 sources with [N II] 3σ detections is log ([N II]/H α) $= -0.47 \pm 0.02$, compatible with the value obtained from the stacked spectrum of the whole sample of 135 bright spectroscopic emitters (log ([N II]/H α) $= -0.52 \pm 0.01$). Finally, we computed the distribution of rest-frame EWs of H α (EW(H α)) and its mean (Fig. 9), obtaining log [EW (H α)/Å] $= 2.08 \pm 0.03$, similar to the result from stacking (log [EW(H α)/Å] $= 2.05 \pm 0.01$). Adopting the median, a Gaussian model of the distribution, or a 3σ-clipped average does not impact the results. These values are consistent with recent compilations of high-redshift galaxies at similar masses (i.e. Fumagalli et al. 2012; Mármol-Queraltó et al. 2016).

4.2 Optical and near-IR photometry

The tail of bright H α emitters from the FMOS-COSMOS sample is fairly bright in the observed optical and near-IR bands. In Fig. 10, we show the relation between the H α fluxes and *HST*/ACS i_{814}, and the UltraVISTA-DR2 *Y*-, *J*-, *H*-band MAG_AUTO magnitudes for the COSMOS photometric sample (Laigle et al. 2016) and the subset of objects spectroscopically confirmed with FMOS. For reference, the emitters with expected H α fluxes $\geq 2 \times 10^{-16}$ erg cm^{-2} s^{-1} in the COSMOS field have $H < 22.5$ mag. The contours representing the whole photometric sample of SFGs in COSMOS show that our flux predictions capture the scatter of the spectroscopic observations, whilst correctly reproducing the slope of the relations in each band. Note that, by construction, the FMOS-COSMOS selection prioritizes bright galaxies to ensure a high detection rate of emission lines.

4.3 Rest-frame UV sizes

We further attempted to estimate the typical sizes of bright H α emitters. In order to increase the statistics of bright emitters and not to limit the analysis to spectroscopically confirmed objects, we selected a subsample of 750 SFGs in COSMOS with *predicted* H α fluxes $\geq 2 \times 10^{-16}$ erg cm^{-2} s^{-1} (2 per cent of the total photometric sample). The insets in Fig. 1 show the normalized distributions of photometric redshifts and stellar masses for this subsample. Bright emitters follow the same redshift distribution of the whole population, whilst being fairly massive ($\langle \log(M_\star/M_\odot) \rangle = 10.7 \pm 0.4$). Note that all bright emitters in COSMOS lie well above the stellar mass completeness threshold. This is consistent with the fact that we do not find any SFG on the MS in GOODS-S with a predicted H α flux $\geq 2 \times 10^{-16}$ erg cm^{-2} s^{-1} at any mass below our COSMOS completeness limit of $M_\star = 10^{9.8}$ M$_\odot$.

Since we do not have direct access to the spatial distribution of the H α flux, we measured the sizes in the *HST*/ACS i_{814} band, corresponding to rest frame ~3100 Å at $z = 1.55$. Note that given the result on *f*, the attenuation of H α and in the i_{814} band are expected to be nearly identical. We present the analysis for the 750 emitters with *predicted* H α flux $\geq 2 \times 10^{-16}$ erg cm^{-2} s^{-1}, but the results do not change if we consider only the spectroscopic subsample from the FMOS-COSMOS survey. First, we extracted 15 arcsec × 15 arcsec cutouts from the COSMOS archive and we visually inspected them. Considering that the area covered by the *HST*/ACS follow-up is smaller than the whole COSMOS field and excluding strongly contaminated sources, we worked with 649 objects in total. We show a collection of the latter in Appendix A. Given their clumpy morphology, we recentred the cutouts on the barycenter of the light found by SExtractor (Bertin & Arnouts 1996), allowing for a small fragmentation and smoothing over large scales. The final results do not change if we centre the images on the peak of the light distribution. We, then, stacked the cutouts computing their median to minimize the impact of asymmetries and irregularities.

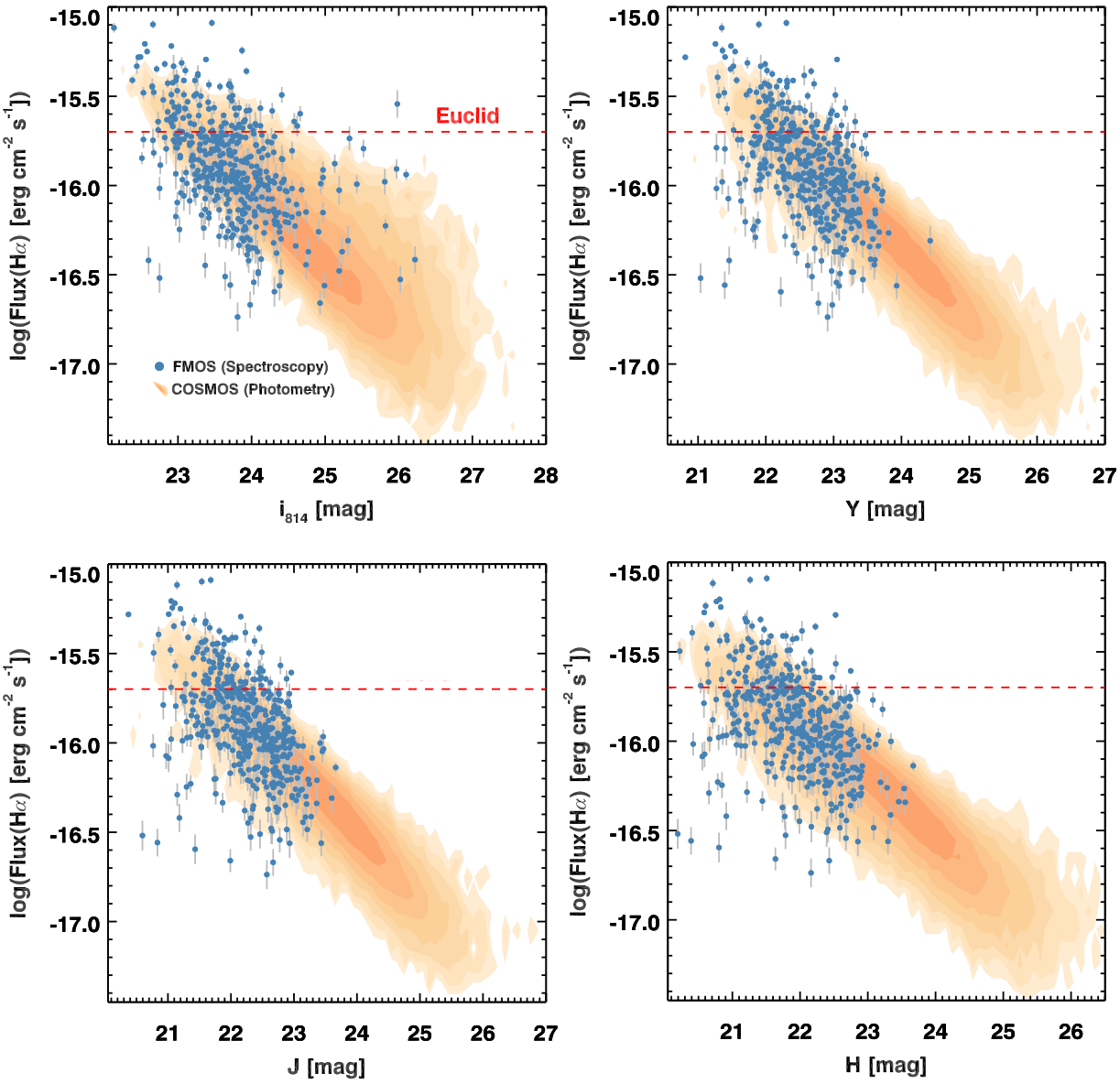

Figure 10. Photometric properties of the COSMOS sample of SFGs at $z \sim 1.5$. The panels show the relation between the Hα fluxes and the *HST*/ACS *i* band (top left), *Y*-band (top right), *J*-band (bottom left), and *H*-band (bottom right) magnitudes from UltraVISTA-DR2. Orange contours represent the whole photometric COSMOS sample and the predicted Hα fluxes. Blue points indicate the subset of objects confirmed by FMOS and their spectroscopic Hα fluxes. Grey bars mark the 1σ uncertainties on the observed Hα fluxes. The red dashed line marks the limit of 2×10^{-16} erg cm^{-2} s^{-1} expected for the Euclid wide survey.

We finally measure the effective radius with a curve of growth, obtaining $R_e = (0.48 \pm 0.01)$ arcsec (∼4 kpc at $z = 1.55$, Fig. 11). The uncertainty is obtained bootstrapping 1000 times the stacking procedure and extracting the curve of growth. To confirm this estimate, we used GALFIT (Peng et al. 2010a) to model the 2D light distribution with a Sersić profile, leaving all the parameters free to vary. To extract a meaningful size directly comparable with the previous estimate, we measured the effective (half-light) radius of the PSF-deconvolved profile, obtaining $R_{\rm GALFIT} = 0.46$ arcsec. The R_e value is comparable with the effective radius of SFGs on the average mass-size relations in literature (i.e. median circularized $R_{\rm e,circ} = 3.4$–3.0 kpc, semimajor axis $R_{\rm semimajor} \sim 4.7$–$4.1$ kpc for late-type galaxies with $\log(M_\star/M_\odot) = 10.75$ at $z = 1.25$–1.75, van der Wel et al. 2014).

5 NUMBER COUNTS OF LINE EMITTERS

We compute the projected cumulative number counts of line emitters at $z \sim 1.5$ starting from the photometric samples in COSMOS and GOODS-S. We base the counts on the *predicted* Hα, [O III] and [O II] fluxes as detailed above. Then, we model the evolution of the number counts of Hα emitters with cosmic time, a crucial step in preparation of forthcoming large spectroscopic surveys with Euclid (Laureijs 2009) and WFIRST (Green et al. 2012; Spergel

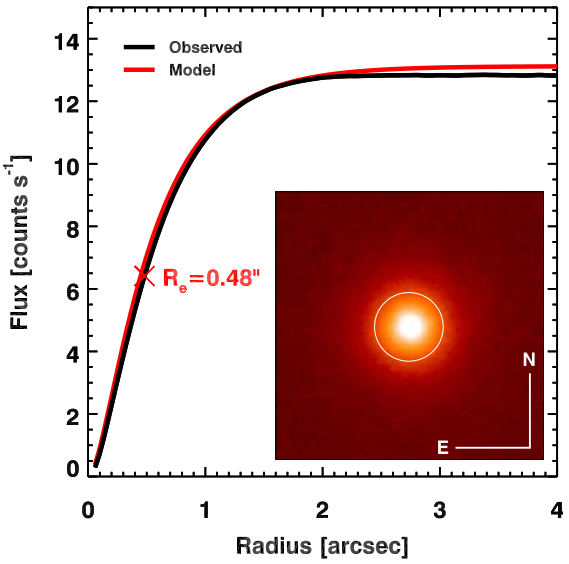

Figure 11. Median *HST*/ACS i_{814} image of bright H α emitters and its curve of growth. The black line represents the curve of growth of the median image of 649 galaxies from the FMOS-COSMOS survey with predicted H α fluxes $\geq 2 \times 10^{-16}$ erg cm^{-2} s^{-1}. The red line shows the result of the 2D light decomposition with GALFIT, including the deconvolution of the PSF. The red cross marks the effective radius. The inset shows the 3.75 arcsec $\times$ 3.75 arcsec median stacked image. The white circle indicates the effective radius $R_e = 0.48$ arcsec. It also roughly corresponds to the 'optimal' aperture size maximizing the signal-to-noise ratio for the detection ($R = 0.43$ arcsec, Section 6.4).

et al. 2015). Our method has the advantage of fully exploiting the large number statistics of current photometric surveys and it complements the classical approach based on a spectroscopic data set and the modelling of the evolution with redshift of the H α luminosity functions (Geach et al. 2010; Pozzetti et al. 2016). A detailed analysis of the H α LF for the FMOS-COSMOS survey is deferred to future work (Le Fèvre et al., in preparation).

5.1 H α emitters: the FMOS-COSMOS redshift range

First, we computed the cumulative number counts for the redshift range of $1.4 < z < 1.8$ covered by the FMOS-COSMOS survey, starting from the COSMOS and GOODS-S photometric samples spread over an area of 1.57 and 0.054 deg^2, respectively. The cumulative number counts are reported in Table 1 and shown in Fig. 12. We computed the uncertainties on the cumulative counts both as Poissonian 68 per cent confidence intervals and from simulations. In order to capture the sample variance, we bootstrapped 1000 mock samples of the same size of the observed one, randomly extracting objects from the photometric samples, allowing for any number of duplicates. We, then, recomputed the number counts for each mock sample and estimated the uncertainties as the standard deviation of their distribution for each flux. We further simulated the impact of the cosmic variance on small angular scales counting galaxies in areas of 0.26 deg^2 (1/6 of the total surface covered by the COSMOS photometric sample) and 0.054 deg^2, taken randomly in the COSMOS field. We, then, added these contributions in quadrature.

Furthermore, we included the effect of the uncertainties on the predicted H α fluxes on the final estimate of the number counts, as necessary to fairly represent their scatter. These uncertainties naturally spread out the counts in a flux bin to the adjacent ones.

Table 1. Cumulative number counts of H α emitters from the COSMOS and GOODS-S photometric samples.

Flux limit (10^{-16} erg cm^{-2} s^{-1})	COSMOS									GOODS-S							
		$1.4 < z < 1.8$				$0.9 < z < 1.8$				$1.4 < z < 1.8$				$0.9 < z < 1.8$			
	Average[a]	σ_{conv}[b]	$\sigma_{P,68}$[c]	σ_{MC}[d]	Average	σ_{conv}	$\sigma_{P,68}$	σ_{MC}	Average	σ_{conv}	$\sigma_{P,68}$	σ_{MC}	Average	σ_{conv}	$\sigma_{P,68}$	σ_{MC}
	(deg^{-2})	(deg^{-2})	(deg^{-2})	(deg^{-2})	(deg^{-2})	(deg^{-2})	(deg^{-2})	(deg^{-2})	(deg^{-2})	(deg^{-2})	(deg^{-2})	(deg^{-2})	(deg^{-2})	(deg^{-2})	(deg^{-2})	(deg^{-2})
≥ 0.10	–	–	–	–	–	–	–	–	31635	$\pm$ 195	$\pm$ 776	$\pm$ 2485	69400	$\pm$ 449	$\pm$ 1140	$\pm$ 5053
≥ 0.25	–	–	–	–	–	–	–	–	16936	$\pm$ 99	$\pm$ 573	$\pm$ 2024	39661	$\pm$ 18	$\pm$ 869	$\pm$ 4239
≥ 0.50	9318	$\pm$ 78	$\pm$ 78	$\pm$ 250	21422	$\pm$ 357	$\pm$ 118	$\pm$ 576	8467	$\pm$ 344	$\pm$ 404	$\pm$ 1207	20999	$\pm$ 582	$\pm$ 629	$\pm$ 2776
≥ 0.75	5671	$\pm$ 231	$\pm$ 59	$\pm$ 132	13994	$\pm$ 310	$\pm$ 93	$\pm$ 342	5107	$\pm$ 270	$\pm$ 316	$\pm$ 675	12809	$\pm$ 745	$\pm$ 488	$\pm$ 1709
≥ 1.0	3555	$\pm$ 324	$\pm$ 46	$\pm$ 86	9328	$\pm$ 594	$\pm$ 75	$\pm$ 216	3225	$\pm$ 326	$\pm$ 249	$\pm$ 425	8487	$\pm$ 702	$\pm$ 396	$\pm$ 1094
≥ 1.5	1490	$\pm$ 327	$\pm$ 28	$\pm$ 50	4468	$\pm$ 643	$\pm$ 50	$\pm$ 118	1524	$\pm$ 250	$\pm$ 172	$\pm$ 216	4283	$\pm$ 552	$\pm$ 280	$\pm$ 554
≥ 2.0	706	$\pm$ 228	$\pm$ 18	$\pm$ 26	2301	$\pm$ 545	$\pm$ 34	$\pm$ 68	823	$\pm$ 177	$\pm$ 128	$\pm$ 104	2421	$\pm$ 429	$\pm$ 210	$\pm$ 296
≥ 2.5	364	$\pm$ 152	$\pm$ 12	$\pm$ 15	1262	$\pm$ 419	$\pm$ 24	$\pm$ 40	481	$\pm$ 131	$\pm$ 100	$\pm$ 63	1471	$\pm$ 337	$\pm$ 163	$\pm$ 165
≥ 3.0	199	$\pm$ 102	$\pm$ 8	$\pm$ 10	737	$\pm$ 304	$\pm$ 17	$\pm$ 24	309	$\pm$ 88	$\pm$ 84	$\pm$ 38	958	$\pm$ 253	$\pm$ 133	$\pm$ 100
≥ 3.5	114	$\pm$ 70	$\pm$ 6	$\pm$ 7	449	$\pm$ 219	$\pm$ 13	$\pm$ 16	208	$\pm$ 60	$\pm$ 72	$\pm$ 25	655	$\pm$ 190	$\pm$ 112	$\pm$ 64
≥ 4.0	69	$\pm$ 47	$\pm$ 4	$\pm$ 4	284	$\pm$ 159	$\pm$ 10	$\pm$ 11	140	$\pm$ 47	$\pm$ 62	$\pm$ 18	460	$\pm$ 148	$\pm$ 95	$\pm$ 43
≥ 4.5	44	$\pm$ 32	$\pm$ 3	$\pm$ 3	187	$\pm$ 114	$\pm$ 7	$\pm$ 8	94	$\pm$ 39	$\pm$ 54	$\pm$ 13	336	$\pm$ 114	$\pm$ 84	$\pm$ 32
≥ 5.0	29	$\pm$ 22	$\pm$ 3	$\pm$ 2	126	$\pm$ 84	$\pm$ 6	$\pm$ 6	76	$\pm$ 20	$\pm$ 54	$\pm$ 8	254	$\pm$ 87	$\pm$ 76	$\pm$ 25
≥ 7.5	5	$\pm$ 4	$\pm$ 1	$\pm$ 1	25	$\pm$ 19	$\pm$ 3	$\pm$ 2	11	$\pm$ 11	–	–	73	$\pm$ 34	$\pm$ 27	$\pm$ 5

Note. The lower and upper (convolved, 'broad') counts shown in Fig. 12 can be obtained subtracting and adding the absolute error σ_{conv} to the counts reported in the "Average" column.
[a]Mean of the convolved and unconvolved number counts (Section 5.1).
[b]Absolute error associated with the convolution of the lower counts with a Gaussian curve 0.19 dex wide ([convolved counts − unconvolved counts]/2, Section 5.1).
[c]Poissonian 68 per cent confidence interval of the unconvolved counts. The naturally asymmetric Poissonian uncertainties have been round up to the highest value between the lower and upper limits.
[d]Monte Carlo bootstrap uncertainties on the unconvolved counts.

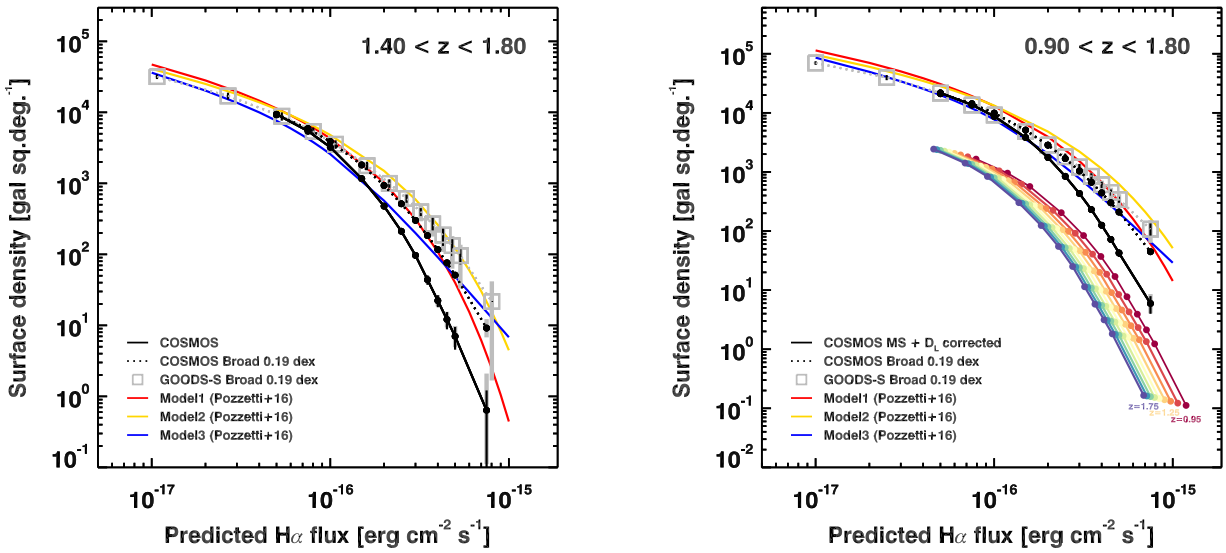

Figure 12. Cumulative Hα counts. Left: Cumulative number counts in the redshift range of $1.4 < z < 1.8$. The Hα fluxes are predicted from the photometry. The solid black line marks the cumulative counts for the COSMOS sample, integrated over the full redshift range. Grey bars indicate the Poissonian 68 per cent confidence interval. Black bars show the 1σ uncertainty on cumulative counts from bootstrap and Monte Carlo simulations. The dotted black line marks the upper limit on cumulative counts, including the uncertainty on the predicted fluxes, causing a broadening of the original values. Grey squares and error bars show the upper limit on the cumulative counts for the GOODS-S photometric sample and their 1σ uncertainties. The red, golden and blue solid lines mark Models 1, 2 and 3 by Pozzetti et al. (2016). Right: Cumulative number counts in the redshift range $0.9 < z < 1.8$ covered by the forthcoming Euclid mission. Coloured lines mark the cumulative counts in $dz = 0.1$ redshift slices (Section 5.2). Other lines and symbols follow the same scheme of the left-hand panel. *Note*. The lower and upper (convolved, 'broad') counts can be obtained subtracting and adding the absolute error $\sigma_{\rm conv}$ to the 'average' counts in Table 1.

In presence of an asymmetric distribution of galaxies in the flux bins, this causes a net diffusion of objects in a specific direction: in this case, from low towards high fluxes. This happens because of the negative, steep slope reached in the brightest flux bins, simply meaning that there are many more emitters at low fluxes than at the high ones. Neglecting the uncertainties on the predicted fluxes would, thus, result in an underestimate of the number counts at high fluxes, since the low-flux population dominates over the bright tail. Note that this is relevant in our calculations, given the relatively large uncertainty also in the brightest flux tail, whilst this is generally not an issue for well determined total fluxes (i.e. with narrow-band imaging or, in principle, grism spectroscopy, but see Section 6.4). The typical flux error is $\sigma_{\rm pred} = 0.1$ dex, obtained subtracting in quadrature the error associated with the total observed Hα flux from FMOS-COSMOS ($\sigma_{\rm obs} = 0.17$ dex, dominated by aperture corrections) from the dispersion of the distribution of H$\alpha_{\rm obs}$/H$\alpha_{\rm pred}$ flux ratios ($\sigma = 0.19$ dex, Fig. 3). Uncertainties related to SED modelling and intrinsic scatter both contribute to this dispersion (Section 3.1). To simulate the diffusion of galaxies from low to high fluxes, we convolved the counts per flux bin with a Gaussian curve of fixed width $\sigma_{\rm broad}$ in the logarithmic space, renormalizing for the initial counts per flux bin. Finally, we recomputed the cumulative counts, now broadened by the errors on predicted fluxes. Adopting the most conservative approach, we set $\sigma_{\rm broad} = 0.19$ dex, as if all the dispersion of the distribution of H$\alpha_{\rm obs}$/H$\alpha_{\rm pred}$ were due to the uncertainty on H$\alpha_{\rm pred}$. This procedures returns a strong upper limit on the cumulative number count estimate, increasing the original values for the COSMOS photometric sample by a factor of $\sim$3 at Hα fluxes of 3×10^{-16} erg cm^{-2} s^{-1}, as shown in Fig. 12. In the same figure, we show the results of an identical analysis applied to the GOODS-S photometric sample, along with the modelling of the recent compilation of spectroscopic and narrow-band data and LFs by Pozzetti et al. (2016). All the curves refer to the same redshift range of $1.4 < z < 1.8$. The counts for the COSMOS and GOODS-S samples are fully consistent within the uncertainties down to the COSMOS completeness flux limit of 5×10^{-17} erg cm^{-2} s^{-1}. The deeper coverage of the rest-frame UV range available for GOODS-S allows us to extend the number counts to Hα fluxes of 1×10^{-17} erg cm^{-2} s^{-1}. Below these limits, the convolved number counts in the two fields are lower than the initial ones due to the incompleteness. The cumulative counts are broadly consistent with the empirical models by Pozzetti et al. (2016), collecting several data sets present in the literature. The agreement is fully reached when considering the effect the uncertainties on the flux predictions. In particular, our results best agree with Models 2 and 3, the latter being derived from high-redshift data only, revising the number counts towards lower values than previously estimated (Geach et al. 2010). Note that our selection includes only colour-selected normal SFGs. Other potentially bright Hα emitters, such as low-mass starbursting galaxies and AGN, might further enhance the final number counts (Section 6).

5.2 Hα emitters: redshift evolution

In order to compare our results with similar existing and forthcoming surveys covering different redshift ranges, we modelled the time evolution of expected Hα fluxes and counts. Our parametrization includes two main effects regulating the Hα flux emerging from star formation in galaxies:

(i) The increasing normalization of the MS with redshift as $(1 + z)^{2.8}$ (Sargent et al. 2014): high-redshift sources are intrinsically brighter in Hα due to higher SFRs at fixed stellar mass.
(ii) Fluxes decrease as the luminosity distance $D_{\rm L}^2(z)$.

The mass–metallicity relation also evolves with redshift, but its effects on the dust content of galaxies are compensated by the increase of the gas fraction, so that the mass–extinction relation mildly depends on redshift (Pannella et al. 2015). Moreover, the

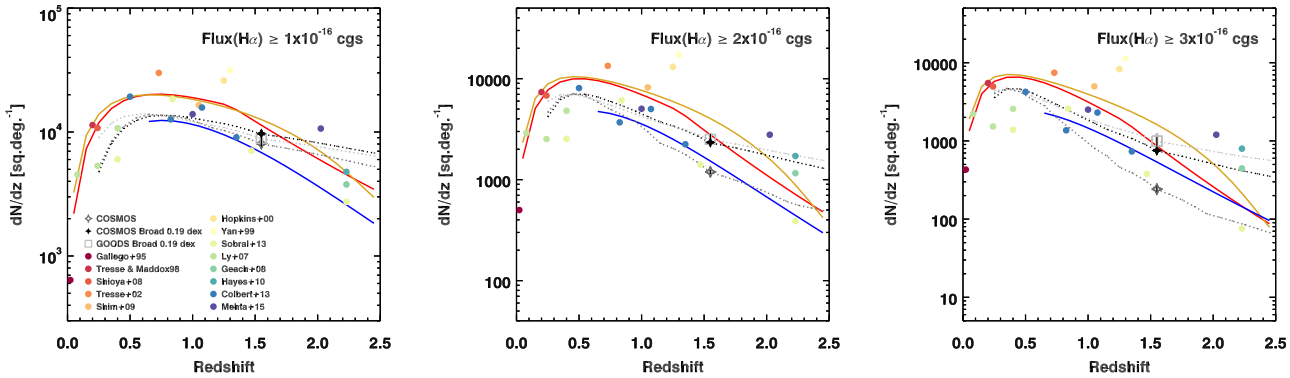

Figure 13. Differential H α counts. The dark grey empty star marks the differential counts dN/dz from the photometric sample in COSMOS. The black filled star corresponds to the upper limit on the counts, including the uncertainty on the predicted fluxes. The light grey empty square indicates the upper limit on the counts for the GOODS-S sample. Grey vertical bars indicate the Poissonian 68 per cent confidence interval. Black bars show the 1σ uncertainty on cumulative counts from bootstrap and Monte Carlo simulations. The dark grey dotted line represents the dN/dz counts for the COSMOS sample. The black and light grey dotted lines show the upper limits on the dN/dz counts for the COSMOS and GOODS-S samples, respectively. The red, golden and blue solid lines mark Models 1, 2 and 3 by Pozzetti et al. (2016). Individual points from the literature in the compilation by Pozzetti et al. (2016) are displayed as filled circles. Differential counts for predicted H α fluxes $\geq 1 \times 10^{-16}$, $\geq 2 \times 10^{-16}$ and $\geq 3 \times 10^{-16}$ erg cm^{-2} s^{-1} are shown in the left-hand, centre and right-hand panels, respectively.

stellar mass function of SFGs is roughly constant from $z \sim 2$ (i.e. Peng et al. 2010b; Ilbert et al. 2013). Therefore, these contributions and other secondary effects (i.e. a redshift-dependent IMFs) are not included in the calculation.

For reference, we computed the cumulative number counts integrated on the redshift range of $0.9 < z < 1.8$ that will be probed by the Euclid mission. First, we assigned the cumulative H α counts from the COSMOS photometric sample to the redshift slice $1.5 < z < 1.6$, enclosing the average redshift probed by the survey $\langle z \rangle = 1.55$, and we rescaled them for the volume difference. Then, we split the calculation in redshift steps of d$z = 0.1$, rescaling the H α fluxes for each redshift slice by $(1+z)^{2.8}/D_{\rm L}^2(z)$ and for the volume enclosed. Note that rescaling the H α fluxes effectively corresponds to a shift on the horizontal axis of Fig. 12, whilst the volume term acts as a vertical shift. To compute the counts over the full redshift range, we interpolated the values in the d$z = 0.1$ slices on a common flux grid and added them. We notice that modelling the evolution of the total H α fluxes with redshift increases by a factor of $\sim$1.5 the cumulative counts for fluxes above $\geq 2 \times 10^{-16}$ erg cm^{-2} s^{-1} obtained simply rescaling for the volume difference the results for the COSMOS photometric sample to the redshift range of $0.9 < z < 1.8$. However, this increase might be partially balanced by an increasing fraction of massive galaxies becoming quiescent. Finally, we convolved the integrated counts with a 0.19 dex wide Gaussian to account for the uncertainty on the predicted H α fluxes (assumed to be comparable with the one derived at $1.4 < z < 1.8$), obtaining an upper limit of the number counts. We calculated uncertainties as Poissonian 68 per cent confidence intervals and with bootstrap and Monte Carlo techniques as detailed in Section 5.1. We show the results of our modelling in Fig. 12, along with the empirical curves by Pozzetti et al. (2016) and the number counts for the GOODS-S photometric sample, obtained applying the same redshift rescaling as in COSMOS. When accounting for the uncertainties on H α fluxes, calculations for both COSMOS and GOODS-S photometric samples are in agreement with the models by Pozzetti et al. (2016) predicting the lowest counts over the $0.9 < z < 1.8$ redshift range. In this interval, we expect $\sim$2300 galaxies deg^{-2} for H α fluxes $\geq 2 \times 10^{-16}$ erg cm^{-2} s^{-1}, the nominal limit for the Euclid wide survey, and 8500–9300 galaxies deg^{-2} from the GOODS-S and COSMOS field, respectively, at a limit of $\geq 1 \times 10^{-16}$ erg cm^{-2} s^{-1}, the baseline depth for WFIRST. Integrating over $1.1 < z < 1.9$, similar to the formal limits of the WFIRST H α survey, we expect $\sim$6200–6800 galaxies deg^{-2} above $\geq 1 \times 10^{-16}$ erg cm^{-2} s^{-1} for the GOODS-S and COSMOS fields, respectively, in agreement with previous estimates (Spergel et al. 2015) within the uncertainties.

The consistency with empirical models and data sets in literature and the importance of including the uncertainties of the predicted H α fluxes are further confirmed by computing the differential counts dN/dz, shown in Fig. 13. These estimates are relevant for the forthcoming redshift surveys and complement the cumulative counts shown in Fig. 12 and reported in Table 1. The three panels show the broad agreement between the evolution of number counts we predict based on the simple modelling of the MS and the public data at different H α fluxes. For these plots, we extended our calculations to the redshift interval $0.2 < z < 2.5$. At lower redshift, a large number of the most massive and brightest H α emitters are likely to quench with time, causing an overestimate of counts. On the other hand, the uncertainties on the evolution of the f factor with time and the increasing contribution of dust obscured SFGs to the overall formation of new stars at $z > 2.5$ limit the analysis above this threshold. However, the evolution of the normalization of the MS is enough to reproduce the growth and drop of the expected H α counts over several Gyrs of cosmic time. Notice that we calculated the upper limits in each redshift slice convolving with a Gaussian curves of fixed width of 0.19 dex as detailed in the previous section.

5.3 [O II] and [O III] number counts at $1.4 < z < 1.8$

We computed the number counts of oxygen line emitters based on the [O II] and [O III] flux predictions in the redshift range of $1.4 < z < 1.8$. We applied the same method described in Section 5.1, keeping into account the uncertainties on the predicted fluxes convolving the number counts with Gaussian curves of fixed width. Results are shown in Fig. 14 and reported in Table 2. The [O III] number counts are roughly consistent with the results from the WISP survey presented in Colbert et al. (2013), once (i) rescaling for the volume and the luminosity distance is properly

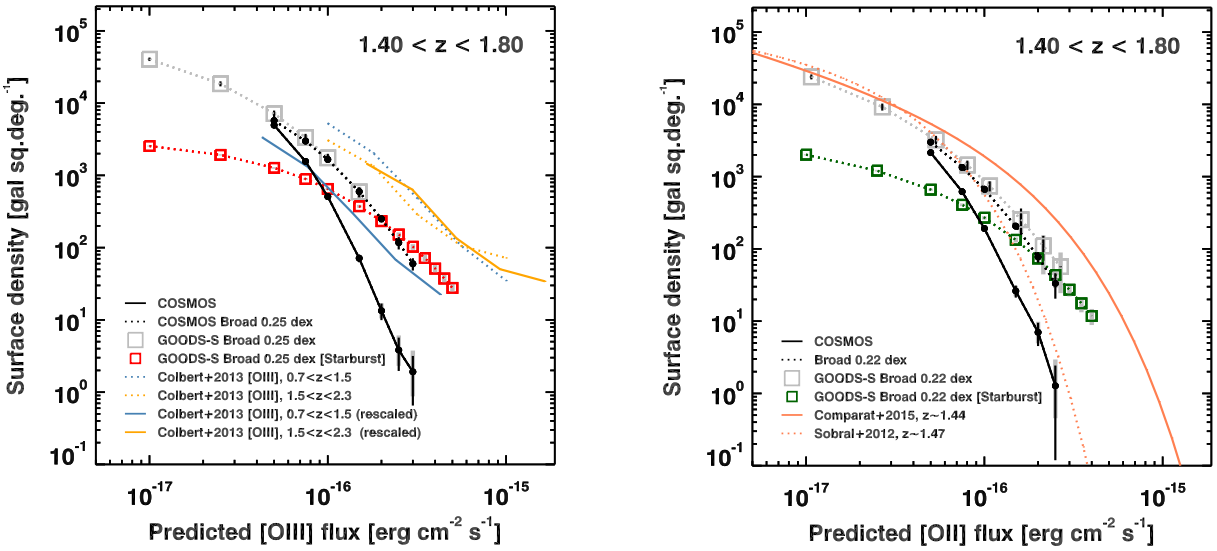

Figure 14. Oxygen line emitters number counts. Left: Cumulative number counts of [O III] emitters in the redshift range of $1.4 < z < 1.8$. The solid and dotted black lines mark the COSMOS cumulative counts and the upper limits keeping into account the uncertainties on predicted fluxes. Grey squares indicate the upper limit on counts in GOODS-S. Red squares represent the upper limit on counts of simulated starbursting galaxies in GOODS-S. Grey bars indicate the Poissonian 68 per cent confidence interval. Black bars show the 1σ uncertainty on cumulative counts from bootstrap and Monte Carlo simulations. Yellow and blue dotted lines show the [O III] counts from the WISP survey by Colbert et al. (2013). Yellow and blue solid tracks show the same counts, but properly rescaled to match the cosmic volume within $1.4 < z < 1.8$ and the luminosity distance at $z \sim 1.55$. Right: Cumulative number counts of [O II] emitters in the redshift range of $1.4 < z < 1.8$. The solid and dotted black lines mark the COSMOS cumulative counts and the upper limits keeping into account the uncertainties on predicted fluxes. Grey squares indicate the upper limits counts in GOODS-S. Green squares represent the upper limit on counts of simulated starbursting galaxies in GOODS-S. Error bars are coded as in the left-hand panel. The orange solid and dotted lines indicate the estimate derived integrating the luminosity functions in Comparat et al. (2015) and Sobral et al. (2012) at $z \sim 1.45$ and assuming their validity over the redshift range of $1.4 < z < 1.8$. *Note*. The lower and upper (convolved, 'broad') counts can be obtained subtracting and adding the absolute error $\sigma_{\rm conv}$ to the 'average' counts in Table 2.

taken into account, and (ii) low-mass galaxies are included in the calculation. Our estimates fall between the WISP counts in the $0.7 < z < 1.5$ and $1.5 < z < 2.3$ intervals. Given how we predict [O III] fluxes (Section 3.3), the increase of the average [O III]/H β ratios and of the MS normalization with redshift can explain the offset between our estimates and Colbert's et al. (2013). Moreover, low-mass galaxies play a critical role, since they have intrinsically higher [O III]/H β ratios. In fact, bright [O III] emitters in the WISP survey are generally low mass ($M_\star \sim 10^{8.5}$–$10^{9.5}$ $M_\odot$; Atek et al. 2011; Henry et al. 2013). The low-mass regime is also sensitive to the presence of high sSFR, unobscured, starbursting galaxies; thus, we expect them to be relevant for the [O III] number counts. We simulated their impact on the counts from the GOODS-S sample as detailed in Section 6.3, and we found a substantial extension of counts above 1.5×10^{-16} erg cm^{-2} s^{-1}, the limit we reach when counting normal MS galaxies (Fig. 14). Starbursting galaxies are expected to reach [O III] fluxes of 3×10^{-16} erg cm^{-2} s^{-1}. In the interval $1.4 < z < 1.8$, we expect ~1100 and ~150 galaxies deg^{-2} above $\geq 1 \times 10^{-16}$ and $\geq 2 \times 10^{-16}$ erg cm^{-2} s^{-1}, averaging the results for the COSMOS and GOODS-S fields. Including the effect of low-mass starburst, we expect ~1700 galaxies deg^{-2} for [O III] fluxes above $\geq 1 \times 10^{-16}$.

For what concerns the number counts of [O II] emitters, the contribution of low-mass galaxies and the different mass completeness limits explain the difference between the COSMOS and GOODS-S samples. The number counts, we derived fall in the range of recent estimates at $z \sim 1.45$ by Sobral et al. (2012) and Comparat et al. (2015). We derived these counts integrating their LFs assuming their validity over the redshift range of $1.4 < z < 1.8$ and for fluxes up to 3×10^{-16} erg cm^{-2} s^{-1}, the limit of our estimates. We divided the counts by Comparat et al. (2015) by ln(10) to account for the different normalizations of the two LFs. Our calculations are in agreement with the estimates by Sobral et al. (2012) up to $\sim 1 \times 10^{-16}$ erg cm^{-2} s^{-1}, whilst we find higher counts above this threshold (a factor 2–3.5 × at $\sim 2 \times 10^{-16}$ erg cm^{-2} s^{-1} considering our 'average' estimate reported in Table 2 for COSMOS and GOODS-S, respectively). On the other hand, we systematically find less counts than in Comparat et al. (2015), a factor of 4.5–4 × (3–2.5 ×) at $\sim 1 \times 10^{-16}$ erg cm^{-2} s^{-1} and 11–6.5 × (6–4.5 ×) at $\sim 2 \times 10^{-16}$ erg cm^{-2} s^{-1} considering the 'average' estimates (the broadened counts) for COSMOS and GOODS-S, respectively. We note that the LF by Comparat et al. (2015) probes only the tail of the brightest emitters, finding a larger number of them than what extrapolated by a fit at lower fluxes by Sobral et al. (2012, see fig. 13 in Comparat et al. 2015). Part of the discrepancy we find is due to the correction for the extinction of the Galaxy that Comparat et al. (2015) applied, whilst we report purely observed and dust reddened fluxes. Moreover, the different sample sizes of Sobral et al. (2012) and Comparat et al. (2015), and our work might affect the results in the poorly populated tail of bright emitters. Over the redshift range of $1.4 < z < 1.8$, we expect 2600 (2700) and ~400 (~500) galaxies deg^{-2} based on the COSMOS (GOODS-S) field 'average' estimate for [O II] fluxes of $\geq 5 \times 10^{-17}$ and $\geq 1 \times 10^{-16}$ erg cm^{-2} s^{-1} (Table 2). These fluxes correspond to ~8σ and ~15σ detection thresholds expected for the PFS survey in the same redshift range (Takada et al. 2014). When including the effect of low-mass starbursting galaxies (Section 6.3), we, thus, expect ~3400 and ~700 galaxies deg^{-2} at fluxes of $\geq 5 \times 10^{-17}$ and $\geq 1 \times 10^{-16}$ erg cm^{-2} s^{-1}, as derived from the average counts in GOODS-S in the range of $1.4 < z < 1.8$.

Table 2. Cumulative number counts of [O II] and [O III] emitters from the COSMOS and GOODS-S photometric samples in the redshift range of $1.4 < z < 1.8$.

Flux limit (10^{-16} erg cm^{-2} s^{-1})	COSMOS									GOODS-S							
		[O II]λ 3727 Å				[O III]λ 5007 Å					[O II]λ 3727 Å				[O III]λ 5007 Å			
	Average[a] (deg^{-2})	$\sigma_{\rm conv}$[b] (deg^{-2})	$\sigma_{\rm P,68}$[c] (deg^{-2})	$\sigma_{\rm MC}$[d] (deg^{-2})	Average (deg^{-2})	$\sigma_{\rm conv}$ (deg^{-2})	$\sigma_{\rm P,68}$ (deg^{-2})	$\sigma_{\rm MC}$ (deg^{-2})	Average (deg^{-2})	$\sigma_{\rm conv}$ (deg^{-2})	$\sigma_{\rm P,68}$ (deg^{-2})	$\sigma_{\rm MC}$ (deg^{-2})	Average (deg^{-2})	$\sigma_{\rm conv}$ (deg^{-2})	$\sigma_{\rm P,68}$ (deg^{-2})	$\sigma_{\rm MC}$ (deg^{-2})
$\geq$0.10	–	–	–	–	–	–	–	–	23727	$\pm$ 317	$\pm$ 672	$\pm$ 2016	41401	$\pm$ 968	$\pm$ 898	$\pm$ 2415
$\geq$0.25	–	–	–	–	–	–	–	–	8705	$\pm$ 527	$\pm$ 405	$\pm$ 1071	17874	$\pm$ 668	$\pm$ 579	$\pm$ 1653
$\geq$0.50	2573	$\pm$ 426	$\pm$ 37	$\pm$ 77	5342	$\pm$ 388	$\pm$ 57	$\pm$ 129	2729	$\pm$ 495	$\pm$ 221	$\pm$ 386	6084	$\pm$ 1062	$\pm$ 322	$\pm$ 676
$\geq$0.75	981	$\pm$ 362	$\pm$ 20	$\pm$ 28	2272	$\pm$ 711	$\pm$ 32	$\pm$ 40	1093	$\pm$ 354	$\pm$ 135	$\pm$ 137	2385	$\pm$ 963	$\pm$ 180	$\pm$ 271
$\geq$1.0	431	$\pm$ 239	$\pm$ 12	$\pm$ 16	1083	$\pm$ 574	$\pm$ 19	$\pm$ 25	482	$\pm$ 261	$\pm$ 84	$\pm$ 74	1079	$\pm$ 673	$\pm$ 106	$\pm$ 133
$\geq$1.5	116	$\pm$ 90	$\pm$ 5	$\pm$ 5	334	$\pm$ 262	$\pm$ 7	$\pm$ 9	163	$\pm$ 90	$\pm$ 58	$\pm$ 22	332	$\pm$ 259	$\pm$ 58	$\pm$ 41
$\geq$2.0	42	$\pm$ 35	$\pm$ 3	$\pm$ 2	132	$\pm$ 118	$\pm$ 4	$\pm$ 3	73	$\pm$ 37	$\pm$ 48	$\pm$ 9	–	–	–	–
$\geq$2.5	17	$\pm$ 16	$\pm$ 2	$\pm$ 1	60	$\pm$ 57	$\pm$ 2	$\pm$ 2	38	$\pm$ 19	$\pm$ 42	$\pm$ 1	–	–	–	–
$\geq$3.0	–	–	–	–	31	$\pm$ 29	$\pm$ 2	$\pm$ 1	–	–	–	–	–	–	–	–

Note. The lower and upper (convolved, 'broad') counts shown in Fig. 14 can be obtained subtracting and adding the absolute error $\sigma_{\rm conv}$ to the counts reported in the "Average" column.
[a]Mean of the convolved and unconvolved number counts (Section 5.1).
[b]Absolute error associated with the convolution of the lower counts with Gaussian curves 0.22 and 0.25 dex wide for [O II] and [O III], respectively ([convolved counts − unconvolved counts]/2, Section 5.1).
[c]Poissonian 68 per cent confidence interval of the lower counts. The naturally asymmetric Poissonian uncertainties have been round up to the highest value between the lower and upper limits.
[d]Monte Carlo bootstrap uncertainties on the lower counts.

6 DISCUSSION

In the previous sections, we showed how it is possible to estimate number counts of line emitters using solely the photometric information and a calibration sample of spectroscopically confirmed objects, reaching a precision at least comparable with the one achieved with standard approaches, generally based on small spectroscopic samples and extrapolations of the LFs. We computed the number counts for the redshift slice $1.4 < z < 1.8$ covered by our calibration sample from the FMOS-COSMOS survey and we extended our calculation for the Hα emitters to the $0.9 < z < 1.8$ interval probed by the Euclid mission, as a reference. We now envisage possible caveats and developments of this work.

6.1 The effect of [N II] lines on low resolution spectroscopy

In Section 5, we computed the galaxy number counts based on the aperture-corrected Hα fluxes only. However, future slitless spectroscopy will not be able to resolve the [N II]–Hα complex, resulting in a boost of galaxy number counts when the [N II] flux is high. In Section 4.1, we found an average line ratio of $\log([{\rm N\,II}]/{\rm H}\alpha) \sim -0.5$ for the bright emitters observable by Euclid, and we provided a simple parametrization of the relation between $\log([{\rm N\,II}]/{\rm H}\alpha)$ and the total observed Hα fluxes (Fig. 9). This relation can be extended at higher redshift, but it must be taken with caution, being naturally affected by observational biases (Kashino et al. 2017a). We, thus, model the effect of the [N II] flux boost fitting a first-order polynomial relation to the FMOS-COSMOS observed $\log(M_\star/{\rm M}_\odot)$–$\log([{\rm N\,II}]/{\rm H}\alpha)$ relation (sample 1, table 2, fig. 14 in Kashino et al. 2017a) and applying a mass-dependent correction to each source. We show the results on the number counts in Fig. 15. We extended the number counts to the $0.9 < z < 1.8$ interval, assuming the same correction. Note that the redshift evolution of the mass–metallicity relation (i.e. Steidel et al. 2014; Sanders et al. 2015) might impact this correction.

We report in Table 3 the counts for Hα+[N II] emitters. The flux boost due to unresolved [N II] emission increases by a factor of $\sim$1.8 × ($\sim$1.6×); the Hα number counts above 2×10^{-16} erg cm^{-2} s^{-1} in the range of $1.4 < z < 1.8$ ($0.9 < z < 1.8$), as derived from the average counts both in the COSMOS and GOODS-S fields.

6.2 The AGN contribution

Strong line emitters such as AGN or starbursting galaxies might increase the number counts as well. We flagged and excluded from our COSMOS sample known *Chandra* detected sources in the catalogue by Civano et al. (2016), since we could not reliably predict Hα fluxes based on their photometry. However, considering only the *Chandra* sources with an estimate of the photometric redshift by Salvato et al. (in preparation), $\sim$17 per cent of the X-ray-detected sample by Civano et al. (2016) (671/4016 galaxies) lie at $1.4 < z < 1.8$, corresponding to 471 objects per deg^2 in this redshift range. This represents a minimal fraction of the overall population of SFGs composing our COSMOS photometric sample (31 193 objects in total). On the other hand, the colour selection we adopted does not prevent low luminosity or obscured AGN to be included in the final sample. Moreover, the FMOS-COSMOS selection function did include some X-ray-detected AGN (Silverman et al. 2015). However, only 11 galaxies in the *Chandra* catalogue by Civano et al. (2016) are detected as Hα emitters with fluxes $\geq 2 \times 10^{-16}$ erg cm^{-2} s^{-1}, representing a fraction of 8 per cent of the overall bright FMOS-COSMOS sample. Therefore, X-ray AGN should not

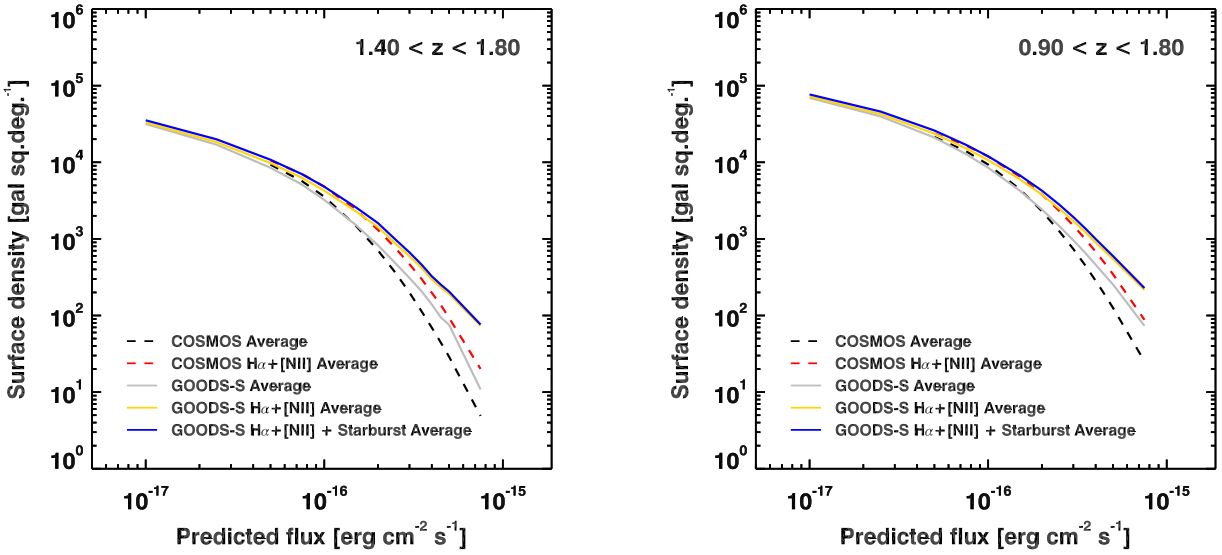

Figure 15. Effect of unresolved [N II] emission and starbursting galaxies on H α counts. The dashed black and red lines mark the H α and H α+[N II] counts average estimate in the COSMOS field, respectively (Tables 1 and 3). The solid grey and yellow lines mark the H α and H α+[N II] counts in the GOODS-S field. The solid blue line indicates the H α+[N II] counts in the GOODS-S field, including the effect of starbursting galaxies (Table 4). Left: FMOS-COSMOS redshift range of $1.4 < z < 1.8$. Right: Full redshift range of $0.9 < z < 1.8$ covered by the forthcoming Euclid mission.

Table 3. Cumulative number counts of H α+[N II] emitters from the COSMOS and GOODS-S photometric samples.

Flux limit (10^{-16} erg cm^{-2} s^{-1})	COSMOS						GOODS-S					
	$1.4 < z < 1.8$			$0.9 < z < 1.8$			$1.4 < z < 1.8$			$0.9 < z < 1.8$		
	H α+[N II][a] (deg^{-2})	σ_{conv}[b] (deg^{-2})	$\sigma_{P,68}$[c] (deg^{-2})	H α+[N II] (deg^{-2})	σ_{conv} (deg^{-2})	$\sigma_{P,68}$ (deg^{-2})	H α+[N II] (deg^{-2})	σ_{conv} (deg^{-2})	$\sigma_{P,68}$ (deg^{-2})	H α+[N II] (deg^{-2})	σ_{conv} (deg^{-2})	$\sigma_{P,68}$ (deg^{-2})
$\geq$0.10	–	–	–	–	–	–	33024	± 144	± 793	72042	± 397	± 1162
$\geq$0.25	–	–	–	–	–	–	18304	± 120	± 595	42435	± 30	± 898
$\geq$0.50	10568	± 122	± 83	23705	± 408	± 124	9767	± 333	± 434	23649	± 571	± 668
$\geq$0.75	7019	± 157	± 66	16620	± 171	± 102	6276	± 257	± 350	15250	± 715	± 534
$\geq$1.0	4813	± 250	± 54	11904	± 441	± 86	4271	± 301	± 288	10700	± 660	± 447
$\geq$1.5	2408	± 304	± 37	6530	± 563	± 62	2300	± 251	± 212	6027	± 530	± 336
$\geq$2.0	1308	± 262	± 26	3796	± 559	± 46	1428	± 154	± 172	3789	± 406	± 267
$\geq$2.5	762	± 204	± 19	2320	± 491	± 35	875	± 173	± 133	2490	± 366	± 216
$\geq$3.0	468	± 154	± 15	1488	± 398	± 27	595	± 133	± 111	1717	± 313	± 179
$\geq$3.5	301	± 114	± 11	992	± 315	± 21	419	± 106	± 96	1224	± 268	± 151
$\geq$4.0	198	± 88	± 9	680	± 249	± 17	297	± 94	± 81	898	± 230	± 130
$\geq$4.5	136	± 65	± 7	480	± 196	± 14	233	± 67	± 75	690	± 182	± 116
$\geq$5.0	93	± 52	± 6	346	± 155	± 12	191	± 44	± 72	547	± 142	± 106
$\geq$7.5	20	± 15	± 3	88	± 52	± 5	73	± 18	± 32	215	± 54	± 55

Notes. [a]Mean of the convolved and unconvolved number counts of H α+[N II] emitters (Section 6.1).
[b]Absolute error associated with the convolution of the lower counts with a Gaussian curve 0.19 dex wide ([convolved counts − unconvolved counts]/2, Section 5.1).
[c]Poissonian 68 per cent confidence interval of the lower counts. The naturally asymmetric Poissonian uncertainties have been round up to the highest value between the lower and upper limits.

provide a significant contribution to the H α number counts at high fluxes in the redshift range of $1.4 < z < 1.8$.

6.3 Starbursting galaxies

Given the large dust attenuation, only few H α photons are expected to escape from massive starbursting galaxies (i.e. lying several times above the MS at fixed redshift). However, at moderate stellar masses ($M_\star \lesssim 10^9$–10^{10} M$_\odot$) galaxies showing high specific SFR (sSFR) and extreme line EWs might contribute to the number counts (Atek et al. 2011). To assess this effect on the cumulative counts of H α emitters, we simulated a population of starbursting galaxies at $M_\star < 10^{10}$ M$_\odot$ artificially increasing their SFRs by a factor of × 4 and considering a volume number density equal to 4 per cent of the one of MS SFGs (Rodighiero et al. 2011). Note that the choice of a mass limit of 10^{10} M$_\odot$ to simulate starburst is conservative, as extreme sSFR and EW in existing slitless spectroscopic surveys occur at $M_\star \sim 10^{8.5}$–$10^{9.5}$ M$_\odot$ (Atek et al. 2011). Since more reliable SFRs are available at low stellar masses in GOODS-S than in COSMOS, we used the GOODS-S for the experiment. We, then, recalculated the H α fluxes and the number densities for the starburst population as in Sections 3.1 and 5. We show the results in Fig. 15 and report the counts for starbursting galaxies in Table 4. The increase of the H α cumulative number counts due to the

Table 4. Cumulative number counts of starbursting emitters from the GOODS-S photometric sample.

Flux limit (10^{-16} erg cm^{-2} s^{-1})	GOODS-S Starburst											
	$1.4 < z < 1.8$									$0.9 < z < 1.8$		
	Hα[a] (deg^{-2})	σ_{conv}[b] (deg^{-2})	$\sigma_{P,68}$[c] (deg^{-2})	[O II][d] (deg^{-2})	σ_{conv}[e] (deg^{-2})	$\sigma_{P,68}$ (deg^{-2})	[O III][f] (deg^{-2})	σ_{conv}[g] (deg^{-2})	$\sigma_{P,68}$ (deg^{-2})	Hα (deg^{-2})	σ_{conv} (deg^{-2})	$\sigma_{P,68}$ (deg^{-2})
≥0.10	2273	±18	±42	2040	±30	±40	2606	±59	±45	4758	±40	±60
≥0.25	1592	±14	±35	1212	±3	±31	1968	±48	±39	3469	±35	±51
≥0.50	1025	±5	±28	636	±23	±22	1271	±2	±31	2324	±1	±42
≥0.75	718	±13	±23	379	±28	±17	861	±29	±25	1667	±28	±35
≥1.0	529	±12	±20	236	±34	±13	602	±47	±21	1256	±31	±31
≥1.5	294	±24	±15	107	±26	±8	327	±48	±15	756	±40	±24
≥2.0	177	±22	±11	55	±19	±6	184	±48	±11	476	±45	±18
≥2.5	109	±20	±9	30	±14	±4	110	±42	±8	311	±44	±15
≥3.0	71	±16	±7	18	±9	±3	70	±33	±6	210	±39	±12
≥3.5	44	±16	±5	11	±7	±2	44	±27	±4	142	±36	±10
≥4.0	28	±14	±4	6	±6	±2	31	±20	±4	98	±32	±8
≥4.5	19	±11	±3	–	–	–	21	±17	±2	70	±27	±6
≥5.0	14	±8	±3	–	–	–	15	±13	±2	51	±22	±5
≥7.5	3	±2	±1	–	–	–	–	–	–	13	±8	±2

Notes. [a]Mean of the convolved and unconvolved number counts of Hα starbursting emitters (Section 6.3).
[b]Absolute error associated with the convolution of the Hα unconvolved counts with a Gaussian curve 0.19 dex wide ([convolved counts −unconvolved counts]/2, Section 5.1).
[c]Poissonian 68 per cent confidence interval of the lower counts. The naturally asymmetric Poissonian uncertainties have been round up to the highest value between the lower and upper limits.
[d]Mean of the convolved and unconvolved number counts of [O II] starbursting emitters.
[e]Absolute error associated with the convolution of the [O II] lower counts with a Gaussian curve 0.22 dex wide.
[f]Mean of the convolved and unconvolved number counts of [O III] starbursting emitters.
[g]Absolute error associated with the convolution of the [O III] lower counts with a Gaussian curve 0.25 dex wide.

low-mass starbursting population is of ∼15 per cent and 20 per cent at 1×10^{-16} erg cm^{-2} s^{-1} and 2×10^{-16} erg cm^{-2} s^{-1}, respectively, at both $1.4 < z < 1.8$ and $0.9 < z < 1.8$. Therefore, our best estimates for Hα number counts including the starbursting population are ∼3800 and ∼1000 (∼9700 and ∼2900) galaxies deg^{-2} in the redshift interval $1.4 < z < 1.8$ ($0.9 < z < 1.8$) for Hα fluxes $\geq 1 \times 10^{-16}$ erg cm^{-2} s^{-1} and $\geq 2 \times 10^{-16}$ erg cm^{-2} s^{-1}, respectively, as evaluated from the average counts in GOODS-S (Tables 1 and 4).

The impact of low-mass starburst on the number counts of [O II] and [O III] emitters is relevant (Fig. 14, Table 4 and Section 5.3). In the redshift range of $1.4 < z < 1.8$, these galaxies increase by ∼50 per cent the number counts derived from MS objects at fluxes $\geq 1 \times 10^{-16}$ erg cm^{-2} s^{-1}.

Finally, we underline that, in order to reach their main scientific goals in cosmology, future spectroscopic surveys need to map the highest possible number of spectroscopic redshifts, irrespectively of which lines are detected. We, thus, collected the cumulative number counts of Hα, [O II] and [O III] emitters in the redshift range of $1.4 < z < 1.8$ at which we calibrated the predicted fluxes. The results are shown in Fig. 16, where we also included the effect of a possible flux boost due to unresolved [N II] emission and the impact of starbursting galaxies as detailed above. We did not attempt to extend these predictions to different redshift ranges, given the uncertainty of the extrapolations of the recipes we adopted to estimate the oxygen emission lines.

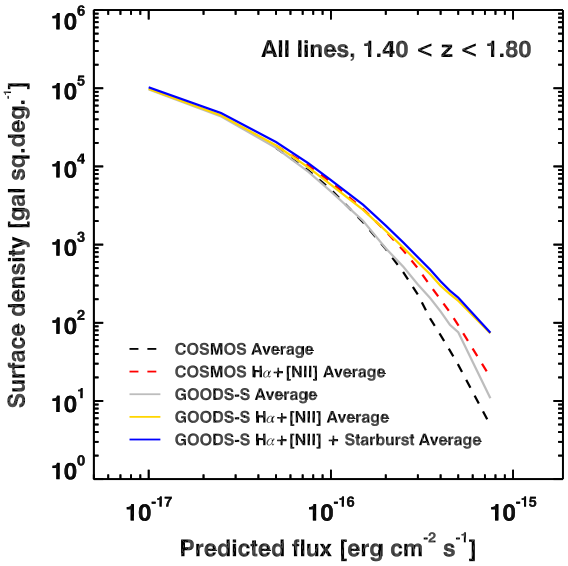

Figure 16. Total cumulative number counts of line emitters at $1.4 < z < 1.8$. The black dashed line indicates the cumulative number counts obtained adding the average estimates of the Hα, [O II], and [O III] emitter counts in the COSMOS field (Tables 1 and 2). The red dashed line shows the counts in COSMOS when taking into account the [N II] unresolved emission ('average' estimates in Table 3). The grey, gold and blue solid lines mark the cumulative counts for emitters in GOODS-S considering (i) Hα, [O II] and [O III] emitters; (ii) including the effect of [N II] unresolved emission as for the COSMOS field; (iii) finally adding the population of low-mass starbursting galaxies (Table 4).

6.4 Estimating a survey effective depth and return

In order to optimize the detectability and, thus, the number of detections for extended objects like galaxies, one has to reach a

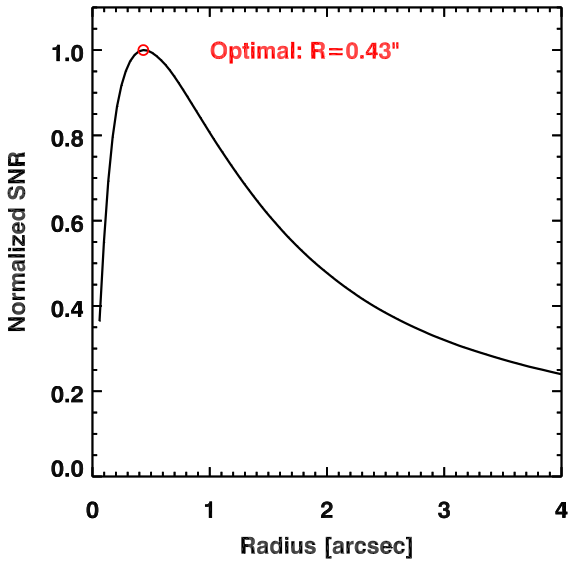

Figure 17. Signal-to-noise ratio in circular aperture photometry of bright Hα emitters. The black line represents the signal-to-noise ratio in circular apertures as a function of their radius for the median *HST*/i_{814} image of bright Hα emitters in Fig. 11. We normalized the curve to its peak. The red circle marks the radius maximizing the signal-to-noise ratio.

compromise between (i) recovering as much as possible of galaxies' flux, which requires large apertures; and (ii) limiting the noise associated with the measurement, obtained minimizing the apertures. This leads to a situation in which the *optimal* aperture is driven by the galaxy surface brightness profile, as discussed in the previous sections. Moreover, flux measurements are necessarily performed in some apertures, and the ensuing flux losses must be taken into account when analysing the performances of a survey. For example, spectroscopic surveys with multi-object long slits or fibres with fixed diameters will be affected by losses outside the physically pre-defined apertures. Aperture corrections introduce further uncertainties on the total flux estimates, thus the effective depth of a survey is shallower in terms of total galaxy flux than what computed inside the aperture. A similar effect also influences slitless spectroscopy: despite providing a high-fidelity 2D map of each emission line in galaxies and allowing for recovering the full flux under ideal circumstances, sources must be first robustly identified before emission line fluxes can be measured. The advantage of slitless spectroscopy is that the size and shape of apertures might in principle be adjusted to the size of each object, not being physically limited by a fibre or slit.

Based on the stacked image of the Hα emitters with fluxes $\geq 2 \times 10^{-16}$ erg cm^{-2} s^{-1} shown in Fig. 11, we estimated the optimal radius for the circular aperture that maximizes its signal-to-noise ratio (Fig. 17). This radius is 0.43 arcsec($\sim$0.9 R_e), causing an aperture loss of a factor of $\sim$2.2$\times$. The flux losses ensuing any aperture measurement imply a higher 'effective' flux limit of a survey – defined as the minimum *total* emission line flux recoverable above a given signal-to-noise detection threshold – than the 'nominal' limit defined in a specific aperture. For example, observations designed to provide secure detections down to a line flux F_{ap} within an aperture of radius $R = R_e \sim 0.5''$ (i.e. the 'nominal' depth) would set an 'effective' depth of $F_{eff} = 2F_{ap}$. This effective depth can be used to assess the 'return' of the survey, i.e. the number of recoverable spectroscopic redshifts, by comparing with the cumulative number counts of galaxies above F_{eff} as in Figs 12 and 14, and Tables 1 and 2. In fact, as common practice, we derived the line fluxes in Section 3 from *integrated*, observed SED properties, thus not taking into account the size of the galaxies. If neglected, aperture losses cause an increase of the effective flux limit with respect to the nominal one and a decrease of the return at any flux. However, given the shape of the number counts, this effect is more pronounced at high than at low fluxes. For reference, the total number of detections for a nominal sensitivity $F_{ap} \geq 2 \times 10^{-16}$ erg cm^{-2} s^{-1} inside a 0.5 arcsec circular aperture would correspond to a decrease by a factor of $\sim$10 of the return when considering the effective depth $F_{eff} = 2F_{ap} \geq 4 \times 10^{-16}$, considering the case of Hα emitters in the COSMOS field (Table 1). On the other hand, for $F_{ap} \geq 5 \times 10^{-17}$ erg cm^{-2} s^{-1}, the return drops by a factor of $\sim$3 when estimating it at the corresponding effective depth $F_{eff} \geq 1 \times 10^{-16}$ erg cm^{-2} s^{-1}. The smaller factor at lower fluxes is due to the flattening of the counts and it could be overestimated, since such weaker emitters likely have typical sizes smaller than we estimated in Section 4.3, resulting in lower flux losses. Note that, when computing counts within fixed apertures, we kept into account the evolution of the intrinsic sizes of SFGs ($R_e \propto (1+z)^{-0.8}$; van der Wel et al. 2014; Straatman et al. 2015) when assessing the effect for redshift intervals larger than $1.4 < z < 1.8$. Moreover, the effect of the PSF of *HST*/ACS is negligible on the estimate of the optimal aperture, whilst it may play a role for ground based and seeing-limited observations.

Adopting apertures larger than the optimal one, the flux losses and the difference between nominal and effective depths are reduced. For example, considering circular apertures of 2 arcsec diameter or, equivalently, rectangular apertures of 1 arcsec $\times$ 3.4 arcsec ($\sim 2R_e \times 7R_e$) would reduce the aperture losses to only a factor of $\sim$1.2, the pseudoslit mimicking the long-slit spectroscopic case and a possible choice for the extraction of slitless spectra. In this case, the effective depth would be only 1.2$\times$ shallower than the nominal depth, and the implied change in return would also be fairly limited (a factor of 1.2–1.6 at 5×10^{-17} and 2×10^{-16} erg cm^{-2} s^{-1}, respectively), if aperture losses are neglected. Note, however, that at fixed integration time, using apertures of any shape, but larger – or smaller – than the optimal one decreases the achievable nominal signal-to-noise ratio, further reducing the return with respect to the optimal case presented above. Doubling the aperture area does not come for free, as it requires a 4$\times$ higher integration time to reach the same flux limit with the same signal-to-noise ratio. Hence, adopting larger apertures for line detection to reduce aperture losses, without adjusting accordingly the exposure time, is not a way to boost the return of a survey, as it instead reduces the return with respect to the optimal case. Following the definitions of 'effective' and 'nominal' depths, any possible combination of flux losses and corresponding survey returns can be estimated using the profile given in Fig. 11 and the cumulative number counts for total fluxes in Figs 12 and 14–16 and Tables 1–4, according to the specific apertures set in each survey. We emphasize that the optimal aperture suggested here ($R \sim 0.5$ arcsec) is rather large by space standards, corresponding to $\sim$5$\times$ the full width half-maximum of *HST*/ACS point spread function.

We warn the reader that several other effects might reduce the possible impact of these findings. First, our sizes are not directly measured on Hα emission line maps, but based on the UV rest-frame proxy, and it is perhaps a surprising finding that aperture losses are so large even with a $R \sim 0.5$ arcsec aperture on images with the typical *HST* spatial resolution. We cannot rule out that individual bright emitters might be more compact than the median we show in Fig. 11, although the attenuation of UV continuum light is expected to be fully comparable to that of Hα, and both are tracing

SFRs. Then, for low-spectral resolution observations, line blending (i.e. [N II]+Hα) will boost the number counts. On the other hand, resolving the emission lines, as it might be expected for long-slit or fibre spectroscopy from the ground, would cause the opposite effect, reducing the signal-to-noise per resolution element. Finally, AGN and starbursting galaxies can further increase the number counts in the brightest tail, considering their expected compact emission and high EW. We caution the reader that this is a simple experiment based on a specific class of bright Hα emitters, with an average radially symmetric shape, a disc-like light profile, and a typical *HST*/ACS point spread function. The effect of seeing and the exact PSF shape of each set of observations can be modelled convolving the profile in Fig. 11, assessing its effect on the optimal aperture. Future simulations might address several open issues with detailed descriptions of the specific characteristics of each survey, which is beyond the scope of this work.

7 CONCLUSIONS

We have shown that fluxes of rest-frame optical emission lines can be reliably estimated for thousands of galaxies on the basis of good-quality multicolour photometry. We have further explored one of the possible applications of having this information for large samples of galaxies, namely to establish number counts and to investigate the observable and physical properties of line emitters that will be observed by cosmological surveys. In particular:

(i) We accurately predicted Hα fluxes for a sample of colour-selected SFGs in COSMOS and GOODS-S at redshift $1.4 < z < 1.8$ based on their SFRs and dust attenuation estimates from SED modelling. These galaxies fairly represent the normal MS population at this redshift. We calibrated the predicted fluxes against spectroscopic observations from the FMOS-COSMOS survey. The statistical uncertainty on the final predicted fluxes is $\sigma_{\rm Pred} \sim 0.1$–$0.2$ dex (Fig. 3).

(ii) We predicted the fluxes of the Hβ, [O II] and [O III] lines applying simple empirical recipes and calibrating with spectroscopically confirmed galaxies from the FMOS-COSMOS survey and data publicly available.

(iii) We computed the cumulative number counts of Hα emitters in the redshift range $1.4 < z < 1.8$, finding a broad agreement with existing data in literature and the empirical curves by Pozzetti et al. (2016) modelling the evolution of the Hα luminosity function with redshift (Fig. 12). We obtain fully consistent results when we properly take into account the uncertainty on the predicted Hα fluxes, effectively enhancing the number counts at large fluxes.

(iv) We extended the Hα number counts to the redshift range of $0.9 < z < 1.8$ covered by future surveys such as Euclid and WFIRST. We adopted a physically motivated approach, modelling the evolution of the MS of galaxies with redshift and including the effect of the luminosity distance on the observed fluxes. This method provides results consistent with models and data sets in literature, whilst returning $\sim$1.5$\times$ higher counts for fluxes up to $\geq 2 \times 10^{-16}$ erg cm^{-2} s^{-1} than a simple volume rescaling.

(v) We argue that the evolution of the MS of galaxies is enough to reproduce the time evolution of the differential number counts dN/dz in the range of $0.2 < z < 2.5$, in good agreement with the current data (Fig. 13).

(vi) We computed the number counts for [O II] and [O III] emitters in the redshift range of $1.4 < z < 1.8$, extending the predictions to low fluxes (Fig. 14). Our estimates of [O III] counts are in agreement with previous works once the effect of low-mass galaxies is taken into account. On the other hand, we revise towards lower values the tail of the brightest [O II] emitters at high redshift.

(vii) We investigated the properties of the typical Hα emitters visible in future wide spectroscopic surveys with observed Hα fluxes $\geq 2 \times 10^{-16}$ erg cm^{-2} s^{-1}. We find them massive ($\langle \log(M_\star/M_\odot) \rangle = 10.7 \pm 0.4$), luminous in observed optical and near-IR bands, and with extended UV sizes ($R_{\rm e} \sim 0.48$ arcsec $= 4$ kpc at $z \sim 1.5$). We estimate average [N II]/Hα ratio and rest-frame EW (Hα) of $\log([{\rm N\,II}]/{\rm H}\alpha) = -0.52 \pm 0.01$ and $\log[{\rm EW(H}\alpha)] = 2.05 \pm 0.01$, respectively.

(viii) We examine caveats and possible extensions of this work, including potential counts boosting or decrease by several factors. Failing at resolving the [N II] emission or the inclusion of AGN and low-mass, unobscured, starbursting galaxies with large sSFR and EW might enhance the counts of bright emitters. The impact of low-mass, high-sSFR galaxies is particularly strong on the number counts of oxygen emitters ($\sim$50 per cent increase for fluxes $\geq 1 \times 10^{-16}$ erg cm^{-2} s^{-1}).

(ix) We further discuss the possible optimization of sources detection and explore the relation between the 'nominal' and 'effective' depths of a set of observations. We show how the latter is relevant to estimate the 'return' of a survey in terms of recoverable spectroscopic redshifts. We find that an 'optimal' circular aperture of $R \sim 0.5$ arcsec maximizes the signal-to-noise ratio, causing a factor of $\sim$2$\times$ flux losses that can correspond to a drop of the return, if neglected.

(x) We release a catalogue containing all the relevant photometric properties and the line fluxes used in this work.

ACKNOWLEDGEMENTS

We acknowledge the constructive comments from the anonymous referee, which significantly improved the content and presentation of the results. We thank Georgios Magdis for useful discussions throughout the elaboration of this work. We also thank Melanie Kaasinen and Lisa Kewley for providing the total [O II] fluxes from their observing programme. This work is based on data collected at Subaru Telescope, which is operated by the National Astronomical Observatory of Japan. The authors wish to recognize and acknowledge the very significant cultural role and reverence that the summit of Mauna Kea has always had within the indigenous Hawaiian community. We are most fortunate to have the opportunity to conduct observations from this mountain. FV acknowledges the Villum Fonden research grant 13160 'Gas to stars, stars to dust: tracing star formation across cosmic time'. AC and LP acknowledge the grants ASI n.I/023/12/0 'Attività relative alla fase B2/C per la missione Euclid' and MIUR PRIN 2015 'Cosmology and Fundamental Physics: illuminating the Dark Universe with Euclid'.

REFERENCES

Abazajian K. N. et al., 2009, ApJS, 182, 543
Arnouts S. et al., 2013, A&A, 558, A67
Atek H. et al., 2011, ApJ, 743, 121
Bertin E., Arnouts S., 1996, A&AS, 117, 393
Blake C. et al., 2011, MNRAS, 418, 1707
Bolzonella M., Miralles J.-M., Pelló R., 2000, A&A, 363, 476
Bruzual G., Charlot S., 2003, MNRAS, 344, 1000
Calzetti D., Armus L., Bohlin R. C., Kinney A. L., Koornneef J., Storchi-Bergmann T., 2000, ApJ, 533, 682
Cardelli J. A., Clayton G. C., Mathis J. S., 1989, ApJ, 345, 245
Chabrier G., 2003, PASP, 115, 763

Cirasuolo M. et al., 2014, in Proc. SPIE Conf. Ser. Vol. 9147, Ground-based and Airborne Instrumentation for Astronomy V. SPIE, Bellingham, p. 91470N
Civano F. et al., 2016, ApJ, 819, 62
Colbert J. W. et al., 2013, ApJ, 779, 34
Comparat J. et al., 2015, A&A, 575, A40
Cullen F., Cirasuolo M., Kewley L. J., McLure R. J., Dunlop J. S., Bowler R. A. A., 2016, MNRAS, 460, 3002
Daddi E. et al., 2007, ApJ, 670, 156
Dawson K. S. et al., 2013, AJ, 145, 10
Fitzpatrick E. L., 1999, PASP, 111, 63
Fumagalli M. et al., 2012, ApJ, 757, L22
Geach J. E. et al., 2010, MNRAS, 402, 1330
Green J. et al., 2012, preprint (arXiv:1208.4012)
Henry A. et al., 2013, ApJ, 776, L27
Ilbert O. et al., 2006, A&A, 457, 841
Ilbert O. et al., 2013, A&A, 556, A55
Jouvel S. et al., 2009, A&A, 504, 359
Juneau S., Dickinson M., Alexander D. M., Salim S., 2011, ApJ, 736, 104
Juneau S. et al., 2014, ApJ, 788, 88
Kaasinen M., Bian F., Groves B., Kewley L. J., Gupta A., 2017, MNRAS, 465, 3220
Kashino D. et al., 2013, ApJ, 777, L8
Kashino D. et al., 2017a, ApJ, 835, 88
Kashino D. et al., 2017b, ApJ, 843, 138
Kennicutt R. C., Jr, 1998, ARA&A, 36, 189
Kewley L. J., Geller M. J., Jansen R. A., 2004, AJ, 127, 2002
Kewley L. J., Dopita M. A., Leitherer C., Davé R., Yuan T., Allen M., Groves B., Sutherland R., 2013, ApJ, 774, 100
Kimura M. et al., 2010, PASJ, 62, 1135
Laigle C. et al., 2016, ApJS, 224, 24
Laureijs R., 2009, preprint (arXiv:0912.0914)
Levi M. et al., 2013, preprint (arXiv:1308.0847)
Lilly S. J. et al., 2007, ApJS, 172, 70
Mármol-Queraltó E., McLure R. J., Cullen F., Dunlop J. S., Fontana A., McLeod D. J., 2016, MNRAS, 460, 3587
Mehta V. et al., 2015, ApJ, 811, 141
Meurer G. R., Heckman T. M., Calzetti D., 1999, ApJ, 521, 64
Noeske K. G. et al., 2007, ApJ, 660, L43
Osterbrock D. E., Ferland G. J., 2006, Astrophysics of Gaseous Nebulae and Active Galactic Nuclei. Univ. Sci. Books, Sausalito, CA
Pannella M. et al., 2015, ApJ, 807, 141
Peng C. Y., Ho L. C., Impey C. D., Rix H.-W., 2010a, AJ, 139, 2097
Peng Y.-j. et al., 2010b, ApJ, 721, 193
Perlmutter S. et al., 1999, ApJ, 517, 565
Pozzetti L. et al., 2016, A&A, 590, A3
Puglisi A. et al., 2016, A&A, 586, A83
Riess A. G. et al., 1998, AJ, 116, 1009
Rodighiero G. et al., 2011, ApJ, 739, L40
Rodighiero G. et al., 2014, MNRAS, 443, 19
Salpeter E. E., 1955, ApJ, 121, 161
Sanders R. L. et al., 2015, ApJ, 799, 138
Sargent M. T. et al., 2014, ApJ, 793, 19
Schmidt B. P. et al., 1998, ApJ, 507, 46
Schreiber C. et al., 2015, A&A, 575, A74
Silverman J. D. et al., 2015, ApJS, 220, 12
Sobral D., Best P. N., Matsuda Y., Smail I., Geach J. E., Cirasuolo M., 2012, MNRAS, 420, 1926
Sobral D. et al., 2015, MNRAS, 451, 2303
Spergel D. et al., 2015, preprint (arXiv:1503.03757)
Steidel C. C. et al., 2014, ApJ, 795, 165
Straatman C. M. S. et al., 2015, ApJ, 808, L29
Takada M. et al., 2014, PASJ, 66, R1
Talia M. et al., 2015, A&A, 582, A80
van der Wel A. et al., 2014, ApJ, 788, 28
Williams R. J., Quadri R. F., Franx M., van Dokkum P., Labbé I., 2009, ApJ, 691, 1879
Zahid H. J. et al., 2014, ApJ, 792, 75

SUPPORTING INFORMATION

Supplementary data are available at *MNRAS* online.

Table B1. Catalogue of relevant SED-derived quantities and emission line flux predictions for the COSMOS sample.
Table B2. Catalogue of relevant SED-derived quantities and emission line flux predictions for the GOODS-S sample.

Please note: Oxford University Press is not responsible for the content or functionality of any supporting materials supplied by the authors. Any queries (other than missing material) should be directed to the corresponding author for the article.

APPENDIX A: INDIVIDUAL BRIGHT H α EMITTERS

We show in Fig. A1 a random selection of Hα emitters with predicted Hα fluxes $\geq 2 \times 10^{-16}$ erg cm^{-2} s^{-1}. The images are in the *HST*/i_{814} band.

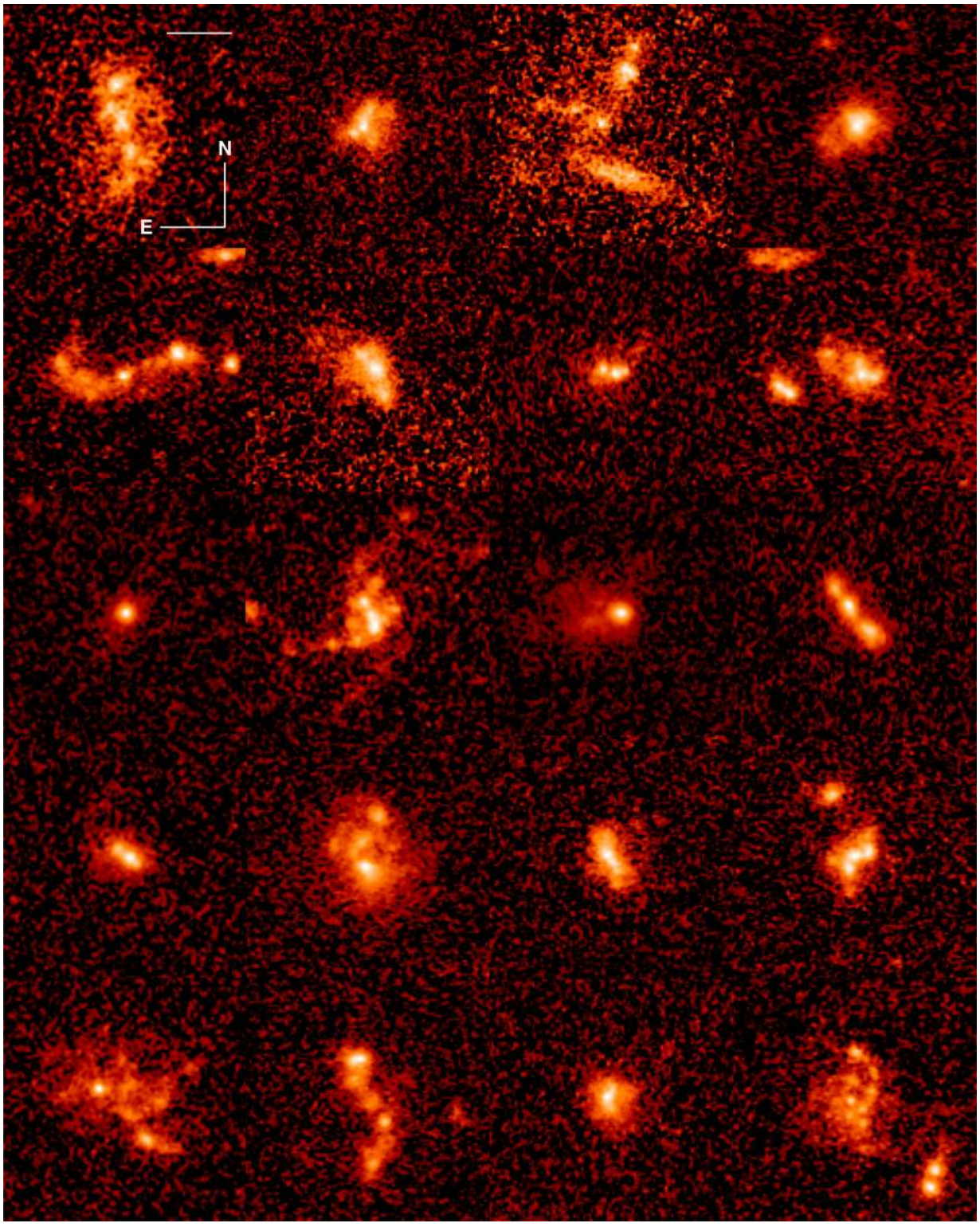

Figure A1. *HST*/i_{814} cutouts of bright Hα emitters in COSMOS. The cutouts show a random sample of emitters with predicted Hα fluxes $\geq 2 \times 10^{-16}$ erg cm^{-2} s^{-1} at $1.4 < z < 1.8$. The size is 3.75 arcsec $\times$ 3.75 arcsec. The images are aligned North-East and they are scaled to the same background level. The white bar shown in the top left-hand panel is 1 arcsec long.

APPENDIX B: CATALOGUE OF LINE FLUXES PREDICTIONS

Table B1. Catalogue of relevant SED-derived quantities and emission line flux predictions for the COSMOS sample (a machine-readable version is available online).

ID[a]	RA (deg)	Dec. (deg)	$\log_{10}(M_\star)$ ($M_\odot$)	$\log_{10}$(SFR) ($M_\odot$ yr^{-1})	$z_{\rm phot}$	$A_{\rm V}$ (mag)	Hα (10^{-16} erg cm^{-2} s^{-1})	[O II] (10^{-16} erg cm^{-2} s^{-1})	[O III] (10^{-16} erg cm^{-2} s^{-1})	Hβ (10^{-16} erg cm^{-2} s^{-1})	$f_{\rm H\beta}$[b]
219860	150.322 350	1.614 831 80	9.69	0.92	1.64	0.70	0.29	0.16	0.27	0.08	1.00
219985	149.984 920	1.614 978 40	9.46	0.58	1.62	0.20	0.23	0.19	0.31	0.07	1.00
220037	149.890 400	1.614 947 10	9.63	0.94	1.63	0.70	0.31	0.17	0.30	0.08	1.00
220136	150.353 750	1.615 008 80	10.45	1.88	1.60	2.00	0.76	0.13	0.19	0.11	1.15
220152	149.759 090	1.615 193 60	9.67	0.78	1.51	0.80	0.24	0.12	0.22	0.06	1.00
...	...	...	...	...	...	...	...	...	...	...	...

Notes. [a]Galaxy ID from (Laigle et al. 2016).
[b]Stellar absorption correction factor (Section 3.2).

Table B2. Catalogue of relevant SED-derived quantities and emission line flux predictions for the GOODS-S sample (a machine-readable version is available online).

ID	RA (deg)	Dec. (deg)	$\log_{10}(M_\star)$ ($M_\odot$)	$\log_{10}$(SFR) ($M_\odot$ yr^{-1})	$z_{\rm phot}$	$A_{\rm V}$ (mag)	Hα (10^{-16} erg cm^{-2} s^{-1})	[O II] (10^{-16} erg cm^{-2} s^{-1})	[O III] [10^{-16} erg cm^{-2} s^{-1}]	Hβ [10^{-16} erg cm^{-2} s^{-1}]	$f_{\rm H\beta}$[a]
1	53.08488800	−27.95581300	9.51	1.40	1.59	1.00	0.71	0.29	0.66	0.16	1.00
2	53.09927000	−27.95315400	9.51	0.55	1.70	0.40	0.15	0.11	0.19	0.05	1.00
3	53.07999000	−27.95205100	10.13	1.02	1.47	1.60	0.20	0.05	0.08	0.03	1.06
4	53.10614800	−27.95160700	9.34	0.96	1.66	0.20	0.52	0.43	0.76	0.17	1.00
5	53.10593400	−27.95165800	9.54	1.14	1.73	0.40	0.58	0.40	0.69	0.17	1.00
6	53.09929700	−27.94932000	8.74	0.17	1.55	0.60	0.07	0.04	0.11	0.02	1.00
...	...	...	...	...	...	...	...	...	...	...	...

Notes. [a]Stellar absorption correction factor (Section 3.2).

This paper has been typeset from a TEX/LATEX file prepared by the author.